

# Structural, optical, and electronic properties of two quaternary chalcogenide semiconductors: $\text{Ag}_2\text{SrSiS}_4$ and $\text{Ag}_2\text{SrGeS}_4$

Garrett C. McKeown Wessler,<sup>1</sup> Tianlin Wang,<sup>1</sup> Jon-Paul Sun,<sup>1</sup> Yuheng Liao,<sup>2</sup> Martin C. Fischer,<sup>2,3</sup> Volker Blum,<sup>1,3</sup> and David B. Mitzi\*,<sup>1,3</sup>

<sup>1</sup>Thomas Lord Department of Mechanical Engineering and Materials Science, <sup>2</sup>Department of Physics, and <sup>3</sup>Department of Chemistry, Duke University, Durham, North Carolina 27708, United States, \*Corresponding author, david.mitzi@duke.edu

## Abstract

Quaternary chalcogenide materials have long been a source of semiconductors for optoelectronic applications. Recent studies on the  $\text{I}_2\text{-II-IV-X}_4$  (I = Ag, Cu, Li; II = Ba, Sr, Eu, Pb; IV = Si, Ge, Sn; X = S, Se) materials have shown particular versatility and promise among these compounds. These semiconductors take advantage of a diverse bonding scheme and chemical differences among cations to target a degree of anti-site defect resistance. Within this set of compounds, the materials containing both Ag and Sr have not been experimentally studied and leave a gap in the full understanding of the family. Here, we have synthesized powders and single crystals of two Ag- and Sr-containing compounds,  $\text{Ag}_2\text{SrSiS}_4$  and  $\text{Ag}_2\text{SrGeS}_4$ , each found to form in the tetragonal  $I\bar{4}2m$  structure of  $\text{Ag}_2\text{BaGeS}_4$ . During the synthesis targeting the title compounds, two additional materials,  $\text{Ag}_2\text{Sr}_3\text{Si}_2\text{S}_8$  and  $\text{Ag}_2\text{Sr}_3\text{Ge}_2\text{S}_8$ , have also been identified. These cubic compounds represent impurity phases during the synthesis of  $\text{Ag}_2\text{SrSiS}_4$  and  $\text{Ag}_2\text{SrGeS}_4$ . We show through hybrid density functional theory calculations that  $\text{Ag}_2\text{SrSiS}_4$  and  $\text{Ag}_2\text{SrGeS}_4$  have highly dispersive band edge states and indirect band gaps, experimentally measured as 2.08(1) and 1.73(2) eV, respectively. Second-harmonic generation measurements on  $\text{Ag}_2\text{SrSiS}_4$  and  $\text{Ag}_2\text{SrGeS}_4$  powders show frequency doubling capabilities in the near-infrared range.

## Introduction

Multinary chalcogenide semiconductors are versatile materials for a wide variety of optoelectronic and energy-conversion applications, including single- and multi-junction photovoltaics (PV),<sup>1,2</sup> photoelectrochemical (PEC) water-splitting,<sup>3,4</sup> thermoelectrics (TE),<sup>5-7</sup> nonlinear optical (NLO) crystals,<sup>8-</sup>

<sup>10</sup> and photonics.<sup>11</sup> The most notable of the commercialized chalcogenide semiconductors are the PV absorbers CdTe and Cu(In, Ga)(S, Se)<sub>2</sub> (CIGSSe), which form the basis of the thin film solar cell market.<sup>12,13</sup> In addition to these examples, the two chalcopyrite semiconductors AgGaS<sub>2</sub> and AgGaSe<sub>2</sub> have gained traction as infrared (IR) NLO crystals with applications for frequency doubling across a wide range of IR wavelengths.<sup>8,9,14–17</sup> The above compounds are based on a zinc-blende-like structural motif in which all cations adopt a similar tetrahedral coordination. Increasing the diversity of the lattice sites (number of distinct sites and associated preferred coordination geometries) in a particular semiconductor can enhance the ability to control properties. Tunability arises not only from a larger number of prospective constituent elements, but also because of opportunities for co-alloying, substitution, or doping with a wider range of elements, providing pathways to shape the materials' electronic structure and a more diverse landscape for fundamental research and property exploration.

Much work has therefore gone into the study of quaternary (and higher-order multinary) chalcogenide semiconductors, with a prime example being Cu<sub>2</sub>ZnSnS<sub>4</sub> (CZTS) and its Se-substituted analog Cu<sub>2</sub>ZnSn(S,Se)<sub>4</sub> (CZTSSe). CZTS(Se) is a prospective replacement PV absorber for CdTe and CIGSSe, as it replaces the toxic (Cd) and scarce (Te, In) elements in these two semiconductors with more abundant and benign alternatives Cu, Zn, and Sn. The quaternaries CZTS and CZTSSe allow for highly tunable optical and electronic properties; however, the application of these compounds is heavily limited by the high level of anti-site disorder among the Cu, Zn and Sn sites in the lattice.<sup>18–20</sup> This issue has been addressed with limited success by off-stoichiometric growth,<sup>21–25</sup> extended and low temperature heat treatments,<sup>26–28</sup> and isoelectronic cationic replacement.<sup>29–33</sup> However, each of these techniques only partially ameliorates the anti-site disorder issue and therefore a new chemical design paradigm is needed to minimize disorder.

Our group and others have recently proposed moving away from this zinc-blende motif and replacing one of the atoms (e.g. Zn in CZTS) with a more chemically distinct ion such as Ba, which tends to adopt a higher coordination number given a larger atomic size.<sup>34–36</sup> The prototype of this new materials family is Cu<sub>2</sub>BaSnS<sub>4</sub> (CBTS), which forms in a trigonal lattice significantly removed from the previously studied tetragonal systems.<sup>37</sup> CBTS and its isostructural Se-substituted analog Cu<sub>2</sub>BaSn(S,Se)<sub>4</sub> (CBTSSe) have been effectively included as absorbers in PV<sup>34,38–43</sup> and PEC<sup>44–51</sup> devices, with significantly reduced cationic disorder as compared to CZTS.<sup>38</sup> The success of CBTS has spurred studies of the wider I<sub>2</sub>-II-IV-X<sub>4</sub> (I = Ag, Cu, Li; II = Ba, Sr, Eu, Pb; IV = Si, Ge, Sn; X = S, Se) materials family for applications beyond photoabsorbers, including TE materials<sup>52–54</sup> and NLO crystals.<sup>55–57</sup> Within this materials family, there is one set of compounds that has not been significantly explored experimentally—i.e. those semiconductors containing Ag and Sr cations. These compounds have previously been theoretically studied, but as of now no experimental syntheses have been reported.<sup>58</sup> In the previous theoretical study, it was predicted that four of these compounds—i.e., Ag<sub>2</sub>Sr(Ge, Sn)(S, Se)<sub>4</sub>—are indirect, narrow band gap semiconductors with

highly dispersive band edges and potential for multivalley semiconductor applications.<sup>58</sup> However, total energy calculations showed nearly indistinguishable differences between two related and possible crystal structures, indicating the need for experimental corroboration of the proper structure type.

Here, we use past surveys of the  $I_2-II-IV-X_4$  family to predict the crystal structures of  $Ag_2SrSiS_4$  and  $Ag_2SrGeS_4$  and to further increase the accuracy of a previously developed tolerance factor approach, i.e. a pair of geometry-based descriptors designed to predict which different possible crystal structures form for particular members of the broader quaternary family.<sup>58–60</sup> We have synthesized powders and single crystals of these two semiconductors, finding that they are isostructural and form in the noncentrosymmetric tetragonal space group  $I\bar{4}2m$ , like previously studied compounds  $Ag_2BaGeS_4$ ,<sup>61</sup>  $Ag_2BaSiSe_4$ ,<sup>60</sup> and  $Ag_2BaSiS_4$ .<sup>59</sup> During the synthesis of these two new compounds, a secondary phase is often found to co-exist with  $Ag_2SrSiS_4$  and  $Ag_2SrGeS_4$ , unless the compounds are prepared under Sr-poor conditions. Single crystals of the impurity phase in the  $Ag_2SrSiS_4$ -targeted synthesis have been isolated and identified through single crystal X-ray analysis as  $Ag_2Sr_3Si_2S_8$ ; by comparison to the calculated X-ray diffraction pattern from Ref. 62, the analogous impurity phase in the  $Ag_2SrGeS_4$  synthesis is found to be  $Ag_2Sr_3Ge_2S_8$  (or  $Sr_6Ag_4Ge_4S_{16}$ ).<sup>62</sup> Each of these impurity phases adopt the cubic space group  $I\bar{4}3d$ . The optical and electronic properties of  $Ag_2SrSiS_4$  and  $Ag_2SrGeS_4$  were then evaluated by experimental and theoretical methods. These two semiconductors are shown to have band gap energies of 2.08(1) eV and 1.73(2) eV, respectively. Band structures calculated by hybrid density functional theory (DFT) reveal indirect band gaps and highly dispersive band maxima within each compound, i.e., with low carrier effective masses at each band edge. Finally, the near-IR frequency-doubling characteristics of these systems are examined relative to a  $AgGaS_2$  standard.

## Experimental & Computational Methods

*Compound synthesis & composition analysis:* Bulk powders of the two title compounds were synthesized by mixing Ag (99.95%, Alfa Aesar), SrS (99.995%, Materion), Si (99.95%, Sigma Aldrich) or Ge (99.999%, Alfa Aesar), and S (99.99%, Sigma Aldrich) powders. This was done with the SrS held at 95% ( $Ag_2SrSiS_4$ ) or 90% ( $Ag_2SrGeS_4$ ) of the stoichiometric molar content to avoid the formation of impurity phases. The powders were ground and cold-pressed under a nitrogen atmosphere into pellets. These pellets were then sealed in pre-baked quartz ampoules under a dynamic vacuum of roughly  $5 \times 10^{-6}$  torr. The sealed ampoules were ramped up from room temperature at 30 °C/hour to 700 °C or 600 °C (for  $Ag_2SrSiS_4$  and  $Ag_2SrGeS_4$ , respectively) and annealed for four days before turning the furnace off to cool. After the first heat treatment, roughly 3–5% of the overall pellet mass was lost and a black material was left on the walls of the quartz ampoules (**Figure S1**). The grinding, pressing, and annealing process was repeated to improve phase homogeneity. The further annealing processes did not cause any significant weight or material loss

and the pellets remained intact during the further anneals, in contrast to the first anneal. The stability of the final products was assessed by comparing powder X-ray diffraction (XRD) and reflectance spectra from when the powder samples were first synthesized and after multiple months of storage (~10 months for  $\text{Ag}_2\text{SrGeS}_4$  and ~4 months for  $\text{Ag}_2\text{SrSiS}_4$ ) in a nitrogen purge box with regular air exposure for measurements (**Figure S2**). Small unidentified XRD reflections appear in both the  $\text{Ag}_2\text{SrSiS}_4$  and  $\text{Ag}_2\text{SrGeS}_4$  patterns after extended storage, pointing to minimal sample degradation over this timeframe. Neither reflectance spectrum changes significantly over storage time, with only a minor increase noted in below band gap absorption for  $\text{Ag}_2\text{SrSiS}_4$ , which may be attributed to small amounts of a poorly crystalline or amorphous secondary phase as discussed below.

To verify the composition of the resultant single-phase powders, the elemental concentrations were measured by inductively coupled plasma mass spectrometry (ICP-MS, Agilent 7900). Roughly 5 mg of the  $\text{Ag}_2\text{SrSiS}_4$  and  $\text{Ag}_2\text{SrGeS}_4$  powders were dissolved in 10 mL of HCl (ACS grade) and then diluted with 10 mL of deionized water. A reference sample containing only HCl and deionized water in the same volume ratios was included in the analysis. Digested powder samples were analyzed by ICP-MS (Agilent 7900) for the elements  $^{28}\text{Si}$ ,  $^{74}\text{Ge}$ ,  $^{88}\text{Sr}$  and  $^{107}\text{Ag}$ . All elements were run in either a reaction gas mode ( $\text{H}_2$ : $^{28}\text{Si}$ ) or collision cell mode (He:  $^{74}\text{Ge}$ ,  $^{88}\text{Sr}$  and  $^{107}\text{Ag}$ ) to reduce polyatomic interferences. All standards and samples were diluted into a 2%  $\text{HNO}_3$ /0.5% HCl (v/v) (Fisher Scientific trace metal grade) matrix made with 18.2 M $\Omega$  water prior to analysis. The instrument was calibrated for  $^{28}\text{Si}$ ,  $^{74}\text{Ge}$ ,  $^{88}\text{Sr}$  and  $^{107}\text{Ag}$  prior to sample analysis (0.1–40  $\mu\text{g/L}$  for Ge, Sr, and Ag; 10–1000  $\mu\text{g/L}$  for Si) using a Spex Certiprep standard (mixed element 2A), with the addition of a single source Spex Certiprep Ge standard. Silicon (Ricca Chemical) was calibrated with a separate solution. Internal Standards of  $^{103}\text{Rh}$  and  $^{115}\text{In}$  were monitored to correct for shifts in the analyte signal intensity during the analysis run. The calibration was verified using NIST traceable second source standards. For Sr and Ag, a standard (CRM-TMDW-A) from High Purity Standards was used, while standards purchased from Agilent and VWR were used for Ge and Si, respectively. The digested samples were diluted by a factor of 100 to 5000 to ensure the analytes of interest were within the calibration curve. This analysis measured metal contents (in mg/mL) of the  $\text{Ag}_2\text{SrSiS}_4$  sample as Ag  $11.5 \pm 0.5$ , Sr  $4.4 \pm 0.1$ , and Si  $1.4 \pm 0.2$ . For the  $\text{Ag}_2\text{SrGeS}_4$  powder, the metal contents were Ag  $7.6 \pm 0.5$ , Sr  $2.9 \pm 0.1$ , and Ge  $2.3 \pm 0.2$  mg/mL. These raw values show that both powders adhere to the expected 2:1:1:4 stoichiometry, as the determined metal cation ratios are  $[\text{Ag}]/[\text{Sr} + \text{Si}] = 1.08 \pm 0.09$  and  $[\text{Sr}/\text{Si}] = 1.04 \pm 0.16$  for  $\text{Ag}_2\text{SrSiS}_4$  and  $[\text{Ag}]/[\text{Sr} + \text{Ge}] = 1.03 \pm 0.08$  and  $[\text{Sr}/\text{Ge}] = 1.05 \pm 0.09$  for  $\text{Ag}_2\text{SrGeS}_4$ .

High quality, yellow single crystals of  $\text{Ag}_2\text{SrSiS}_4$  separated naturally during the grinding of the pellet from the powder synthesis. However, crystals of  $\text{Ag}_2\text{SrGeS}_4$  suitably large for single crystal XRD could not be identified in this manner. Single crystal samples of  $\text{Ag}_2\text{SrGeS}_4$  were recrystallized from the synthesized powder in a eutectic 0.4KI-0.6CsI flux. Synthesized powders of  $\text{Ag}_2\text{SrGeS}_4$  were mixed with

KI and CsI in a 1:12.5 molar ratio. The combined material was ground, pressed and sealed as above. The sealed pellet was ramped to the annealing temperature (same as the powder synthesis) at 30 °C/hr and held at this temperature for four days before being cooled to 400 °C at 4 °C/hr. The annealing temperature of Ag<sub>2</sub>SrGeS<sub>4</sub> (600 °C) is above the melting point of the KI/CsI eutectic (~530 °C), creating a liquid medium for the Ag<sub>2</sub>SrGeS<sub>4</sub> crystal growth.<sup>63</sup> The ampoules were then allowed to cool naturally to room temperature. The products were washed with n, n-dimethylformamide (DMF) and sub-millimeter sized yellow-orange crystals could be separated from any remaining halide flux material. A similar halide flux procedure was attempted for Ag<sub>2</sub>SrSiS<sub>4</sub>. However, the main product of the single crystal growth was not Ag<sub>2</sub>SrSiS<sub>4</sub>, but rather an impurity phase found to be Ag<sub>2</sub>Sr<sub>3</sub>Si<sub>2</sub>S<sub>8</sub>, which appears in the form of bulky, pale yellow crystals. Single crystals of Ag<sub>2</sub>Sr<sub>3</sub>Ge<sub>2</sub>S<sub>8</sub> suitable for single crystal XRD could not be isolated in any of the solid-state or halide flux reactions.

*Crystal structure refinement:* Data collections were done on selected crystals of Ag<sub>2</sub>SrSiS<sub>4</sub>, Ag<sub>2</sub>SrGeS<sub>4</sub>, and Ag<sub>2</sub>Sr<sub>3</sub>Si<sub>2</sub>S<sub>8</sub>, using a Rigaku XtaLab Synergy-S with Mo-K $\alpha$  radiation ( $\lambda = 0.71073 \text{ \AA}$ ) at room temperature. The structures of the compounds were solved by intrinsic phasing (Ag<sub>2</sub>SrSiS<sub>4</sub> and Ag<sub>2</sub>SrGeS<sub>4</sub>) or direct methods (Ag<sub>2</sub>Sr<sub>3</sub>Si<sub>2</sub>S<sub>8</sub>) and refined with anisotropic thermal parameters in Olex2 using the SHELXL software package. Each dataset was reduced with an empirical multi-scan absorption correction. The Ag occupancies for Ag<sub>2</sub>Sr<sub>3</sub>Si<sub>2</sub>S<sub>8</sub> were refined as well. PLATON was used to check the final structures and no higher symmetries were found. Refinement parameters and structure data are presented in **Table 1**. Anisotropic displacement parameters for all three compounds appear in **Tables S1–S3**. Selected bond lengths and bond angles are listed in **Tables S4–S7**.

**Table 1.** Structural details and refinement parameters of the single crystals of title compounds Ag<sub>2</sub>SrSiS<sub>4</sub> and Ag<sub>2</sub>SrGeS<sub>4</sub> as well as Ag<sub>2</sub>Sr<sub>3</sub>Si<sub>2</sub>S<sub>8</sub>. For Ag<sub>2</sub>Sr<sub>3</sub>Si<sub>2</sub>S<sub>8</sub>, the occupancies of the two Ag sites have been refined while the occupancies of the Sr, Si, and S sites are fixed at 1, as attempts to include occupancy refinements did not lead to significant changes in their occupancies.

Nominal Formula	Ag <sub>2</sub> SrSiS <sub>4</sub>	Ag <sub>2</sub> SrGeS <sub>4</sub>	Ag <sub>2</sub> Sr <sub>3</sub> Si <sub>2</sub> S <sub>8</sub>
Empirical Formula	Ag <sub>2</sub> SrSiS <sub>4</sub>	Ag <sub>2</sub> SrGeS <sub>4</sub>	Ag <sub>1.91</sub> Sr <sub>3.00</sub> Si <sub>2.00</sub> S <sub>8.00</sub>
Formula weight	459.69	504.19	781.54
Crystal system		Tetragonal	Cubic
Space group		$I\bar{4}2m$	$I\bar{4}3d$
<i>a</i> (Å)			
<i>b</i> (Å)	6.7669(2)	6.8340(1)	14.0267(1)
<i>c</i> (Å)	7.6144(4)	7.6470(2)	
<i>V</i> (Å <sup>3</sup> )	348.67(3)	357.142(14)	2759.73(6)
<i>Z</i>	2	2	8
Calculated density (g/cm <sup>3</sup> )	4.379	4.688	3.762
$\mu$ (mm <sup>-1</sup> )	14.431	18.048	15.528
Reflections measured,	1099, 252, 0.0086	11115, 305, 0.0225	55708, 713, 0.0267

independent, $R_{\text{int}}$			
GOF on $F^2$	1.131	1.170	1.152
$R_I, wR_2 (I > 2\sigma(I))^a$	0.0193, 0.0491	0.0221, 0.0550	0.0266, 0.0693
$R_I, wR_2$ (all data) <sup>a</sup>	0.0193, 0.0491	0.0230, 0.0554	0.0268, 0.0694
Largest diff. peak and hole ( $e \text{ \AA}^{-3}$ )	0.38/−1.02	0.84/−2.04	1.69/−0.86
Flack parameter	−0.005(6)	−0.007(6)	−0.006(3)
Crystal size (mm)	0.057 x 0.067 x 0.070	0.035 x 0.040 x 0.060	0.070 x 0.115 x 0.125

<sup>a</sup> $R_I = F_o - F_c/F_o$  and  $wR_2 = [w(F_o^2 - F_c^2)^2/wF_o^4]^{1/2}$  for  $F_o^2 > 2\sigma(F_o^2)$ .

*Bulk powder characterization:* Powder XRD patterns of the title compounds were measured on a PANalytical Empyrean diffractometer at room temperature using Cu-K $\alpha$  radiation ( $\lambda = 1.5406 \text{ \AA}$ ). Analysis of these XRD patterns was done using the PANalytical HighScore Plus software, including Pawley phase-fitting and lattice constant refinement. Diffuse reflectance spectra were measured on an Enlitech QE-R Quantum Efficiency/Reflectivity system across the wavelength range of 400 nm to 1250 nm. The reflectance spectra were modified by the Kubelka Munk function,  $F(R)$ , where  $F(R) = (1-R)^2/2R$  and  $R$  is the diffuse reflectance. The band gaps were extracted from these modified reflectance data using an indirect band gap Tauc plot, i.e.,  $(hvF(R))^{1/2}$  versus  $hv$ , using the procedure outlined in Ref. 64.

*Nonlinear optics characterization:* As a qualitative comparison of nonlinear optical properties, bulk AgGaS<sub>2</sub> samples were made employing the same solid-state synthesis techniques as used for the Ag<sub>2</sub>SrSiS<sub>4</sub> and Ag<sub>2</sub>SrGeS<sub>4</sub> compounds above, here using Ag<sub>2</sub>S (Alfa Aesar, 99.995%) and Ga<sub>2</sub>S<sub>3</sub> (Alfa Aesar, 99.99%) and reacting the pressed pellet under vacuum at 1030 °C. The second harmonic generation (SHG) intensity of the powder samples (sieved to particles between 120–170  $\mu\text{m}$  in size) were measured using in-house built optics, similar to that described in Ref. 65. A train of short laser pulses at 1800 nm and a repetition rate of 1 kHz was generated by an optical parametrical amplifier (TOPAS, Light Conversion) pumped by 800 nm pulses with pulse lengths of about 100 fs from a Ti:sapphire regenerative amplifier (Spitfire, Spectra Physics). The beam diameter ( $1/e$  intensity) at the sample position was 4.4 mm and the power was 200 mW (1315 mW/cm<sup>2</sup>). The backscattered second harmonic generation signal from the sample was detected by a fiber optic spectrometer (S2000, Ocean Optics).

*First-principles computations:* All calculations in this paper employ the high-precision,<sup>66,67</sup> all-electron code, FHI-aims,<sup>68–71</sup> which uses numeric atom-centered basis functions for numerical discretization of orbitals and densities. FHI-aims includes a linear-scaling approach to evaluate hybrid density functionals.<sup>72,73</sup> The technical choices for the computations reported in this work follow the same approaches and reasoning laid out in our groups' past work on multinary chalcogenides, specifically:<sup>34,38,58,59,74</sup>

- (1) We employed the ‘intermediate’ numerical settings in FHI-aims and the short-range screened hybrid exchange correlation functional HSE06 (HSE: Heyd-Scuseria-Ernzerhof) with standard settings for the

screening parameter,  $\omega = 0.2 \text{ \AA}^{-1}$ , and exchange mixing parameter,  $\alpha = 0.25^{75-77}$  for all computational results reported in the main text of this work. Hybrid functionals are generally known to improve the prediction of band structures and, specifically, predicted fundamental gaps, for the right mathematical reasons.<sup>78</sup> Our previous work has shown that the above "standard settings" of the HSE06 functional tend to yield predicted fundamental gaps that, for I<sub>2</sub>-II-IV-X<sub>4</sub> compounds of the type considered here, lie a few tenths of an eV below those estimated from optical measurements (Tauc plots).<sup>34,38,58,59,74</sup> However, choosing a system-independent set of standard parameters ensures comparability of band structure results across different compounds and in different works.<sup>34,38,58,59,74,76</sup> Therefore, we do not use an empirical fit of the main parameters of the HSE06 functional ( $\alpha$ ,  $\omega$ ) to match specific, experimentally assessed quantities, such as the fundamental gap as estimated from a Tauc plot, for any results reported in the main text of this work. For illustration only, in the Supporting Information (SI, **Figure S10** and **Table S12** as referenced below) we include energy band structures and densities of states calculated for adjusted exchange mixing parameters ( $\alpha$ ) that match the approximate measured band edges of Ag<sub>2</sub>SrSiS<sub>4</sub> and Ag<sub>2</sub>SrGeS<sub>4</sub>, showing that no qualitative changes result compared to the standard HSE06 parameters applied in the main text.

2) In contrast to predictions of the electronic structure, the choice of the underlying computational geometry *does* merit input from experiment if high-quality data is available. As discussed briefly in our earlier work,<sup>58</sup> the geometry underlying a simulation and the computed single particle-like band structure are different observables and different computational approaches can be employed for their prediction. However, even relatively minor geometry errors of the predicted overall geometry in a chalcogenide material can significantly impact the predicted band gap.<sup>34,58,79</sup> For the computational input geometries, we therefore rely on fixed, experimentally determined lattice parameters, which can be obtained with high precision from powder XRD for a given sample. We then computationally relaxed the atomic coordinates within the unit cell until the magnitude of the associated total energy gradients was below  $5 \times 10^{-3} \text{ eV/\AA}$ . The reliance on experimental unit cell parameters is especially relevant for the Ag<sub>2</sub>SrGeS<sub>4</sub> compound that is experimentally found to form in the  $\bar{I}42m$  space group here, while the same compound was predicted to break its symmetry and computationally relax towards the *I222* structure in Ref. 58 (see "Results & Discussion" below). The band structure calculations in the present paper therefore reflect the geometry of the  $\bar{I}42m$  room-temperature experimental structure. Note also that a different k-space path was followed for *I222* compounds compared to  $\bar{I}42m$  in Ref. 58, but key parameters associated with the electronic band structures remain comparable.

The  $\Gamma$ -point-centered k-point grids used for HSE06 calculations and respective fixed lattice parameters are listed in **Table S8**. Band structures were then calculated, including non-selfconsistent spin-orbit coupling (SOC).<sup>80</sup> The first Brillouin zone and the k-space path are illustrated in **Figure S3**. Densities of states

(DOSs) were calculated using the tetrahedron integration method.<sup>81</sup> Normal-incidence absorption coefficients were calculated, using the random phase approximation, from the HSE06+SOC electronic structure and Gaussian broadening with 0.1 eV width to ensure a smooth integration of the imaginary and real components of the dielectric function, similar to our previous work.<sup>58,74,82,83</sup> The calculated absorption coefficients thus cover direct band-to-band transitions at the level of hybrid DFT, intended to provide a qualitative comparison with measured Tauc plots. They do not, however, include phonon-assisted indirect transitions or potential excitonic effects, either of which would be significantly more difficult to capture in a numerically converged way from higher-level methods; such a comparison is not the focus of this paper. We primarily evaluate the computational absorption coefficients to demonstrate that optical anisotropy should exist in the materials studied here. Final geometry files used in these calculations are included at the end of the SI. The bond lengths and angles in the geometries derived from the HSE06+SOC calculations agree closely with those of the reported single crystal structures (**Table S9**).

## Results & Discussion

*Structure prediction and powder X-ray diffraction data:* Previously derived structural tolerance factors for the I<sub>2</sub>-II-IV-X<sub>4</sub> materials family have shown promise for loosely segregating known compounds into distinct regions by crystal structure type and for predicting the crystal structure of hypothetical compounds within this space.<sup>59</sup> Using this empirical tolerance factor approach, as shown in **Figure S4**, Ag<sub>2</sub>SrSiS<sub>4</sub> might be predicted to crystallize in the  $\bar{I}42m$  or the *Ama2*† (Ag<sub>2</sub>PbGeS<sub>4</sub> structure type). Ag<sub>2</sub>SrGeS<sub>4</sub> might be expected to form the *I222* or the *Ama2*† structure types. However, given the proximity of Ag<sub>2</sub>SrGeS<sub>4</sub> to the *t*<sub>IV</sub> tolerance factor range that separates known *I222* and  $\bar{I}42m$  compounds in **Figure S4**, the  $\bar{I}42m$  space group could be consistent with Ag<sub>2</sub>SrGeS<sub>4</sub> as well. As the Ag-containing materials are less explored compared to the Cu-based semiconductors, the region of the plot where these two compounds fall has a low density of data points and is therefore less well-defined. Increasing the number of structurally characterized family members in this region of the phase diagram will increase our understanding of how phase stability depends on the proposed structural tolerance factors. The crystal structure predictions may be further refined based upon past trends within this semiconductor family. Within the Cu- and related Li-containing materials, the tendency within the sulfides is that, when substituting Ba with Sr, there is no phase transition and the Ba- and Sr-based materials are isostructural.<sup>37,84–87</sup> This would suggest that Ag<sub>2</sub>SrSiS<sub>4</sub> and Ag<sub>2</sub>SrGeS<sub>4</sub> may both adopt the  $\bar{I}42m$  structure type (given known Ba-based compounds).<sup>59,61</sup> Synthetic efforts are clearly needed to test these hypotheses.

The new quaternary compounds Ag<sub>2</sub>SrSiS<sub>4</sub> and Ag<sub>2</sub>SrGeS<sub>4</sub> were prepared by traditional solid-state methods (see Experimental section). Using a stoichiometric ratio of reactants, the target compounds are difficult to fully separate from impurity phases, even after probing multiple thermal annealing conditions.

In addition, a black material—identified as  $\text{Ag}_8\text{SiS}_6$  or a mixture of  $\text{Ag}_8\text{GeS}_6$  and  $\text{Ag}_{11}\text{Ge}_3\text{S}_{10}$ —evaporates out of the pellets during the reaction.  $\text{Ag}_8\text{SiS}_6$  has been previously seen as a prevalent secondary phase in syntheses of related compounds  $\text{Ag}_2\text{BaSiS}_4$  and  $\text{Ag}_2\text{PbSiS}_4$ .<sup>59</sup> The evaporation of this Ag-rich phase may leave a Sr-rich environment for the solid-state reaction and hence, impurity phases can form separately from the target  $\text{Ag}_2\text{SrSiS}_4$  and  $\text{Ag}_2\text{SrGeS}_4$ . However, when reacted with reduced SrS content (between 2.5 and 10 molar percent; the amount was determined empirically), the powders can be purified as shown in **Figure S5**, even though the amount of evaporated black material does not change significantly. The purified powders of the title compounds are yellow ( $\text{Ag}_2\text{SrSiS}_4$ ) and yellow-orange ( $\text{Ag}_2\text{SrGeS}_4$ ) in color, with compositions confirmed by ICP-MS (see Methods section above). The XRD peaks of the title compounds all index to those expected for the  $\bar{I}42m$  structure of isostructural  $\text{Ag}_2\text{BaGeS}_4$  (**Figure 1**).  $\text{Ag}_2\text{SrSiS}_4$  and  $\text{Ag}_2\text{SrGeS}_4$  represent just the fourth and fifth semiconductors that share this structure type and the first quaternary chalcogenides in this family containing both Ag and Sr cations. A previous computational study by some of us predicted that  $\text{Ag}_2\text{SrGeS}_4$  will break its symmetry (compared to  $\bar{I}42m$ ) and instead take on lattice parameters and atomic coordinates consistent with the orthorhombic  $I222$  crystal structure when fully relaxing the structure (including unit cell parameters) at the DFT-HSE06 level of theory.<sup>58</sup> In contrast, the experimental powder XRD pattern of  $\text{Ag}_2\text{SrGeS}_4$  is clearly indicative of the  $\bar{I}42m$  structure, as shown by a direct comparison of the experimental data to a simulated XRD stick pattern of the fully relaxed structure of Ref. 58 (**Figure S6**). It is important to note that the  $I222$  space group is only a lower symmetry version of  $\bar{I}42m$  and (as mentioned earlier) the  $\text{Ag}_2\text{SrGeS}_4$  data point in the tolerance factor plot (**Figure S4**) is significantly closer to the  $\bar{I}42m/I222$  boundary than the analogous data point for  $\text{Ag}_2\text{SrSiS}_4$  (the primary difference is found in the tolerance factor  $t_{\text{IV}}$ ). Although we did not pursue low-temperature XRD measurements in this work, it is conceivable that the room-temperature  $\bar{I}42m$  space group found for  $\text{Ag}_2\text{SrGeS}_4$  is a (relatively) high-temperature phase and that the  $I222$  phase may form at lower temperatures (in line with the earlier computational prediction and the tentative location in the tolerance factor plot).

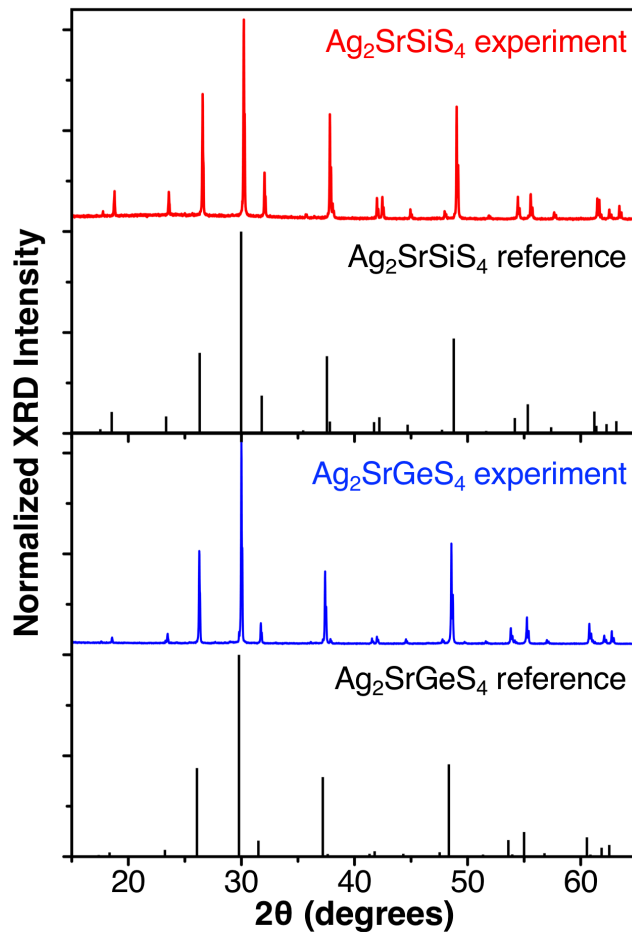


**Figure 1.** Powder X-ray diffraction patterns of  $\text{Ag}_2\text{SrSiS}_4$  and  $\text{Ag}_2\text{SrGeS}_4$  synthesized at a SrS-reduced stoichiometry compared to references (see Methods Section). References are calculated from the refined single crystal structures (described in the next section).

The impurity component noted in **Figure S5** seems to be the same phase across both the  $\text{Ag}_2\text{SrSiS}_4$ - and  $\text{Ag}_2\text{SrGeS}_4$ -targeted reactions (nearly identical powder XRD peaks). During the crystal growth of  $\text{Ag}_2\text{SrSiS}_4$  (solid-state) and  $\text{Ag}_2\text{SrGeS}_4$  (halide flux), these impurity phases separate naturally from the target compound. The impurity phases can be identified by single crystal XRD as  $\text{Ag}_2\text{Sr}_3\text{Si}_2\text{S}_8$  (for the Si-based compound) and by comparing calculated powder XRD patterns as  $\text{Ag}_2\text{Sr}_3\text{Ge}_2\text{S}_8$  (for the Ge-based compound; see **Figure S5**).<sup>62</sup> These two new compounds are II-atom rich quaternary systems related to the previously reported  $\text{Ag}_2\text{Sr}_3\text{Ge}_2\text{Se}_8$  and  $\text{Cu}_2\text{Ba}_3\text{Sn}_2\text{S}_8$ ,<sup>88,89</sup> and form in the cubic space group  $I\bar{4}3d$ , as described for  $\text{Ag}_2\text{Sr}_3\text{Si}_2\text{S}_8$  in **Table 1**. As seen in **Figure S5**, a mixture of  $\text{Ag}_2\text{SrSiS}_4$  ( $\text{Ag}_2\text{SrGeS}_4$ ) and  $\text{Ag}_2\text{Sr}_3\text{Si}_2\text{S}_8$  ( $\text{Ag}_2\text{Sr}_3\text{Ge}_2\text{S}_8$ ) can account for all the reflections seen in the experimental diffraction patterns of the samples prepared from stoichiometric starting reactions. The lattice parameters obtained from a Pawley phase-fitting procedure of the XRD patterns of the powders, grown using both stoichiometric and reduced SrS compositions, show good agreement with each other and with the reported single crystal data

(i.e., compare values in **Tables 1** and **S10**). This comparison shows that there is little to no detectable structural change in the target compounds ( $\text{Ag}_2\text{SrSiS}_4$  and  $\text{Ag}_2\text{SrGeS}_4$ ) when grown from various stoichiometries, as the change in lattice constants between the stoichiometric and SrS-reduced cases falls within experimental resolution. The propensity to form the Sr-rich impurity phases under stoichiometric reaction conditions demonstrates one important reason (in addition to possible loss of  $\text{Ag}_8(\text{Si}/\text{Ge})\text{S}_6$ -related phases during the reaction) why the SrS-reduced stoichiometry reaction is successful in isolating the title compounds, as it provides an unfavorable condition for the formation of the cubic impurity phases. These impurity phases have been presented here to rationalize the need for a SrS-reduced synthesis condition; the cubic compounds and associated properties will be discussed in more detail in a separate paper.

*Single crystal structures of target compounds:*  $\text{Ag}_2\text{SrSiS}_4$  and  $\text{Ag}_2\text{SrGeS}_4$  each form within the noncentrosymmetric, tetragonal space group  $\bar{I}42m$  and, as they are isostructural, the description of the crystal structure will focus on  $\text{Ag}_2\text{SrGeS}_4$ . The refined crystal structure of  $\text{Ag}_2\text{SrGeS}_4$  appears in **Figure 2(a)**. Within the framework of the above-mentioned structural tolerance factor approach,<sup>59</sup> the connectivity between the highly distorted  $[\text{AgS}_4]$  tetrahedra and the  $[\text{SrS}_8]$  dodecahedra is characterized by edge-sharing between  $[\text{AgS}_4]$  and four nearest  $[\text{SrS}_8]$  clusters. This 3D network of  $[\text{AgS}_4]$  tetrahedra and  $[\text{SrS}_8]$  dodecahedra is further decorated and interconnected by isolated, regular  $[\text{GeS}_4]$  tetrahedra to form the entirety of the lattice. These and related structures such as  $\text{Li}_2\text{Ba}(\text{Ge}, \text{Sn})(\text{S}, \text{Se})_4$  have been termed “compressed chalcopyrites” by others due to the strong similarities between these structures and their chalcopyrite relatives.<sup>86</sup> Namely, these similarities include the 3D network of corner-sharing cation tetrahedra, here between the Ag and M (M = Ge, Si) polyhedra. The major difference between these and the chalcopyrites is the same difference that gives this family of materials some unique characteristics, specifically the high coordination number of the third cation, Sr. The demand of the larger cation—e.g. Sr—to have a higher coordination leads to the compression of the chalcopyrite-like lattice and the typical (for these compounds) high level of distortion of the  $[\text{AgS}_4]$  tetrahedra, as compared to the more regular  $[\text{AgS}_4]$  tetrahedra in the chalcopyrites—e.g.,  $\text{AgGaS}_2$  or the related kesterite  $\text{Ag}_2\text{ZnSnS}_4$ .<sup>90,91</sup>

The  $\bar{I}42m$  structure of  $\text{Ag}_2\text{SrGeS}_4$  is further characterized by the placement of the Ag atoms at a special site within the lattice, which distinguishes it from the closely related  $I222$  structure adopted by compounds such as  $\text{Ag}_2\text{BaGeSe}_4$ , where the Ag atoms sit on general sites.<sup>92</sup> In the  $\bar{I}42m$  lattice, the angle between any three Ag atoms when viewed along any principal axis is either  $90^\circ$  or  $180^\circ$  as shown in **Figure S7(a–c)**. However, in the  $I222$  structure—adopted by the related  $\text{Ag}_2\text{BaGeSe}_4$  compound—the Ag atoms are not aligned as such; when viewed along the *a*- and *b*-axes, the Ag atoms take on a zigzag or wave-like pattern (**Figure S7(d, e)**). A last distinguishing feature of the  $\text{Ag}_2\text{SrGeS}_4$  lattice can be seen from **Figures 2(b)** where the Ag atoms within the lattice take on a highly anisotropic thermal ellipsoid along the *c*-direction

(i.e.,  $U_{33} = 0.1099 \text{ \AA}^2$ ). In each of the Ag-containing compounds in this family, all having this distorted tetrahedral bonding arrangement, the  $c$ -direction component of the anisotropic displacement parameter for the Ag atoms is greater than  $0.05 \text{ \AA}^2$ , while those of other atoms are significantly lower.<sup>60,61,92–94</sup> In this bonding coordination (**Figure 2(b)**), the  $[\text{AgS}_4]$  tetrahedra are flattened such that the bonds are nearly coplanar, with two S-Ag-S bond angles of  $149.87(7)^\circ$  and  $93.87(2)^\circ$  for  $\text{Ag}_2\text{SrGeS}_4$ . The crystal structure of  $\text{Ag}_2\text{SrSiS}_4$  is the same as that of  $\text{Ag}_2\text{SrGeS}_4$  (**Figure S8**) and any differences among bond lengths and angles are less than 1.5%, except for the M-S bonds (**Tables S4** and **S5**).  $\text{Ag}_2\text{SrGeS}_4$  and  $\text{Ag}_2\text{SrSiS}_4$  are not only the first Ag-Sr-containing compounds discovered within the  $I_2\text{-II-IV-X}_4$  materials family, but also the first Ag-Sr compounds within the wider “compressed chalcopyrite” systems that exhibit these distinguishing features of aligned Ag atoms and stretched Ag thermal ellipsoids.

The  $\bar{I}42m$  structure identification for both  $\text{Ag}_2\text{SrSiS}_4$  and  $\text{Ag}_2\text{SrGeS}_4$  continues the trend in the  $I_2\text{-II-IV-X}_4$  family that replacement of Ba with Sr does not lead to a structural transition, since  $\text{Ag}_2\text{BaSiS}_4$  and  $\text{Ag}_2\text{BaGeS}_4$  also take on the  $\bar{I}42m$  structure type. From the structural tolerance factor viewpoint, the  $\bar{I}42m$  structure assignment agrees with the prediction for  $\text{Ag}_2\text{SrSiS}_4$ , whereas for  $\text{Ag}_2\text{SrGeS}_4$  (see **Figure S4**), all of  $I222$ ,  $\bar{I}42m$  or  $Ama2^\dagger$  are plausible anticipated structure types. However, the  $I222$  and  $\bar{I}42m$  structures are closely related (see above and **Figure S7**) and the tolerance factors for  $\text{Ag}_2\text{SrGeS}_4$  fall into a sparsely explored region of the tolerance factor plot. The discovery of  $\text{Ag}_2\text{SrGeS}_4$  in the  $\bar{I}42m$  structure demonstrates the flexibility of the  $\bar{I}42m$  structure to tolerate a wide variety of cations. This is similar to the case of the  $P3_1$  structure type adopted by Cu-containing compounds, which spans a wide portion of the structural tolerance factor plot and can include multiple combinations of cations and anions while maintaining the same structure. Further work probing the edges of the structural tolerance factor plot is still needed to fully map the crystal structure space of the  $I_2\text{-II-IV-X}_4$  materials family and to confirm how applicable this approach is on the far-right side of the diagram in **Figure S4**, at which point the compounds no longer have the same connectivity among the metal chalcogenide polyhedra as for those on the left side (for which the tolerance factors were originally derived).

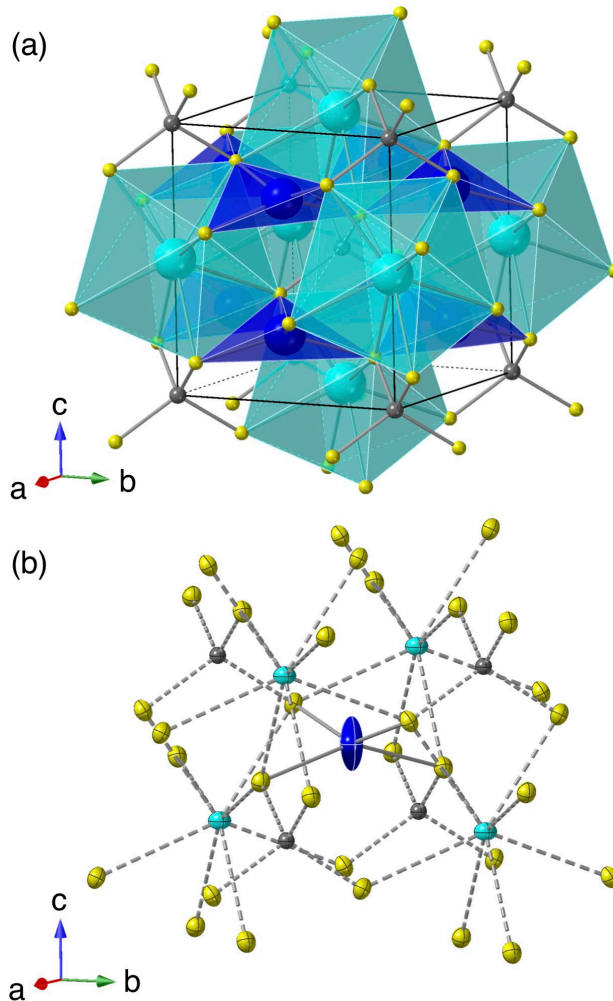


**Figure 2.** (a) Crystal structure of  $\text{Ag}_2\text{SrGeS}_4$  (conventional cell) shown in polyhedral representation (for Ag and Sr). (b) Image showing the anisotropic bonding of Ag within  $\text{Ag}_2\text{SrGeS}_4$ . The Ag, Sr, Ge, and S atoms are colored as blue, cyan, grey, and yellow, respectively. All atoms are shown with anisotropic thermal ellipsoids at 50% probability in panel (b).

*Electronic structure:* DFT-HSE06+SOC calculated band structures and DOS are shown in **Figure 3**, with the DOS plotted on an expanded energy scale and Brillouin zone k-paths depicted in **Figures S9** and **S3**, respectively. The band structures reveal that, similarly to other  $\bar{I}42m$  compounds in this materials space, the lowest energy transition is indirect, here from the Z point to the  $\Gamma$  point. The computed indirect band gap energies are 1.75 eV and 1.38 eV for  $\text{Ag}_2\text{SrSiS}_4$  and  $\text{Ag}_2\text{SrGeS}_4$ , respectively, as listed in **Table 2**. Meanwhile, the energies of the lowest energy direct transitions at the Z point are 2.31 eV and 1.84 eV for the Si- and Ge-containing compounds respectively, a roughly 0.5 eV shift above the indirect transition, which is consistent with our previous calculations of the Ag-based compounds in the  $\text{I}_2\text{-II-IV-X}_4$  material family.<sup>58,59</sup> The calculated indirect band gaps match well with the trends seen in the set of  $\text{I}_2\text{-II-IV-X}_4$  compounds, namely replacing Ba with Sr does not typically lead to a large shift in the band gap energies;

calculated band gaps of the Ba-containing analogs  $\text{Ag}_2\text{BaSiS}_4$  and  $\text{Ag}_2\text{BaGeS}_4$  are 1.96 eV and 1.39 eV, respectively, when calculated using the same functionals, electronic structure code and calculation settings.<sup>58,59</sup> Although  $\text{Ag}_2\text{SrSiS}_4$  and  $\text{Ag}_2\text{SrGeS}_4$  each have indirect band gaps, the band maxima/minima are highly dispersive, suggesting relatively low effective masses (**Table S11**) for each of these compounds as compared to the Cu-substituted analogs. For example,  $\text{Ag}_2\text{SrGeS}_4$  has lower effective masses at each band extremum, especially for the valence band where the effective masses are 25% ( $\parallel a$ ) and 50% ( $\parallel c$ ) lower than the analogous effective masses of  $\text{Cu}_2\text{SrGeS}_4$ .<sup>58</sup>

The band edges of a majority of the compounds within the  $\text{I}_2\text{-II-IV-X}_4$  family are dominated by states associated with I and X elements and the cases of  $\text{Ag}_2\text{SrSiS}_4$  and  $\text{Ag}_2\text{SrGeS}_4$  are no exception. Here, the valence band maxima are composed of hybridized, occupied states of Ag and S. The conduction band minima (CBM) are generally composed of a low density of Ag states and the other three elements start to contribute to the conduction band states as one moves to energies above the CBM for both  $\text{Ag}_2\text{SrSiS}_4$  and  $\text{Ag}_2\text{SrGeS}_4$ . Each of these compounds exhibit multivalley electronic structures, suggesting possible interest for manipulation of the valley degree of freedom<sup>95</sup> and high-performance thermoelectric materials.<sup>96</sup> As noted above, a HSE06-based structure optimization (without experimental input) in an earlier work by some of us predicted that  $\text{Ag}_2\text{SrGeS}_4$  would form in the lower-symmetry orthorhombic  $I222$  space group.<sup>58</sup> The  $\bar{I}42m$  (this work) and  $I222$  structures are closely related and, therefore, key predicted band structure parameters such as the fundamental gap and effective masses are also similar between Ref. 58 and the present work. The  $I222$   $\text{Ag}_2\text{SrGeS}_4$  band structure shown in Ref. 58 follows a different  $k$ -space path than that shown for  $\bar{I}42m$  in the present work, but the band structure calculated for  $\bar{I}42m$   $\text{Ag}_2\text{BaGeS}_4$  in Ref. 58 is overall quite similar to the result for  $\bar{I}42m$   $\text{Ag}_2\text{SrGeS}_4$  shown in **Figure 3(b)**.

The calculated absorption coefficients of  $\text{Ag}_2\text{SrSiS}_4$  and  $\text{Ag}_2\text{SrGeS}_4$  (**Figures 4(a,b)**) exhibit remarkably similar features, albeit shifted by  $\sim 0.4$  eV due to the difference in the materials' band gaps. It is important to recall that these calculated absorption coefficients cannot capture the lowest energy indirect transitions, as phonon effects are not included; therefore, the calculated absorption coefficients cannot be considered to absolutely correspond to experimental absorption data, for which phonon-assisted indirect band-to-band transitions will still contribute. Nevertheless, the calculated absorption coefficients of these tetragonal compounds demonstrate a slight anisotropy along different lattice directions. In both compounds there is a  $\sim 0.1$  eV shift of the absorption onset to higher energies along the  $c$  axis as compared to the  $a$  and  $b$  axes. While this anisotropy is on the order of the Gaussian broadening function used to obtain smooth integration of the dielectric functions, it could have an impact on the light absorption of these materials if integrated into a device. We speculate that the high connectivity of the  $[\text{AgS}_4]$  tetrahedra along the  $a$  and  $b$  directions (and lack of such connectivity along  $c$ ) could cause stronger absorption, as Ag and S are the dominant contributors to the electronic band structures at the band maxima. More generally, the calculated

onset of the direct absorption for each of these compounds is relatively slow. At an energy of 0.5 eV above the lowest energy direct band gap, the absorption coefficient along the  $a$  and  $b$  axes is still three orders of magnitude below the maximum value at higher energies. The slow absorption onset is similar to the previously calculated absorption of the isostructural compound  $\text{Ag}_2\text{BaSiS}_4$ .<sup>59</sup>

For the standard HSE06+SOC parameters  $\omega = 0.2 \text{ \AA}^{-1}$  and  $\alpha = 0.25$ , a shift of a few tenths of an eV between the measured absorption edge and the calculated band gap is typical for multinary chalcogenides of the type studied here.<sup>34,58,59,74</sup> As mentioned in the computational section, it is possible to change the DFT-HSE06 exchange mixing parameter,  $\alpha$ , in order to match the experimentally measured lowest (indirect) optical transition (the experimental data are described in the next section). This procedure leads to  $\alpha$  values of 0.324 and 0.328 for  $\text{Ag}_2\text{SrSiS}_4$  and  $\text{Ag}_2\text{SrGeS}_4$ , respectively, with corresponding electronic structure results shown in **Figure S10** and **Table S12**. The modified  $\alpha$  values do not significantly change the shape of the calculated band edges (**Figure S10**) and result in a slight decrease in the energy difference,  $E_{\text{I-D}}$ , between the lowest energy indirect (I) and direct (D) transitions (**Table S12**). The  $E_{\text{I-D}}$  values of 0.52 eV and 0.40 eV with the optimized  $\alpha$  for  $\text{Ag}_2\text{SrSiS}_4$  and  $\text{Ag}_2\text{SrGeS}_4$ , respectively, are decreased from  $E_{\text{I-D}} = 0.56 \text{ eV}$  and  $0.46 \text{ eV}$  with  $\alpha = 0.25$ .

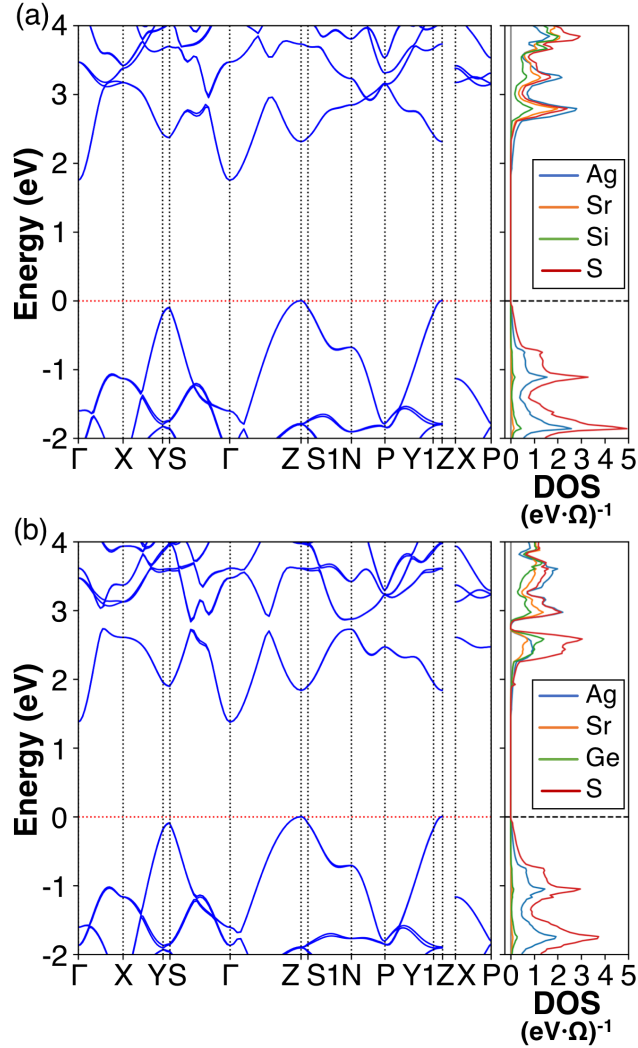


**Figure 3.** Computed band structures and partial density of states (DOS) of (a)  $\text{Ag}_2\text{SrSiS}_4$  and (b)  $\text{Ag}_2\text{SrGeS}_4$  (HSE06 hybrid density functional including spin-orbit coupling).  $\Omega$  is the unit cell volume used in the HSE06 calculations. K-point grids and lattice parameters for the calculations are listed in **Table S8**. The Brillouin zone and k-space paths are shown in **Figure S3**.

*Optical properties:* Diffuse reflectance spectra for the title compounds, modified by the Kubelka-Munk function,  $F(R)$ , and expressed as indirect Tauc plots (**Figure 4(c,d)**), lead to the extracted band gap values listed in **Table 2**. The  $\text{Ag}_2\text{SrSiS}_4$  and  $\text{Ag}_2\text{SrGeS}_4$  powders appear yellow and yellow-orange, respectively, while the extracted band gaps are 2.08(1) eV and 1.73(2) eV, which would typically imply red or dark red colors for both semiconductors. However, the indirect nature of the band structures combined with the low DOS at the band maxima of  $\text{Ag}_2\text{SrSiS}_4$  and  $\text{Ag}_2\text{SrGeS}_4$  yield colors for the synthesized powders that are lighter than those implied by the experimentally extracted (as well as calculated) band gap values. The lighter colors of each compound do agree with the lowest energy direct transition positioned roughly 0.5 eV above the indirect transition as mentioned above. Specifically, if the measured bands gaps are shifted

by 0.5 eV, the new band gaps place each compound into the expected color range—i.e., 2.23 eV corresponds to orange for  $\text{Ag}_2\text{SrGeS}_4$  and 2.58 eV to yellow to yellow-orange for  $\text{Ag}_2\text{SrSiS}_4$ .

The pronounced foot seen in the  $\text{Ag}_2\text{SrSiS}_4$  reflectance spectrum may come from small inclusions of poorly crystalline (such that it resists identification by powder XRD) or glassy Ag-Si-S phases remaining in the synthesized powder, such as amorphous  $\text{Ag}_8\text{SiS}_6$ .<sup>97</sup> It is improbable that this aspect of the absorption spectra is intrinsic to the  $\text{Ag}_2\text{SrSiS}_4$  band structure, as there is no evidence that the band gap should be below the DFT-calculated fundamental gap of 1.75 eV ( $\alpha = 0.25$ ). To confirm the hypothesis that the absorption foot comes from small inclusions of glassy or poorly crystalline  $\text{Ag}_8\text{SiS}_6$ -related phases, we examined, under an optical microscope, powder samples that had been annealed multiple times (**Figure S11(a)**) and could visually observe some black or darkly colored grains on the surface of the expected yellow  $\text{Ag}_2\text{SrSiS}_4$  pellet. We further synthesized crystalline  $\text{Ag}_8\text{SiS}_6$  and could observe that the absorption onset matches quite closely the position of the foot in the reflectance spectrum of  $\text{Ag}_2\text{SrSiS}_4$  as shown in **Figure S11(b)**. Thus, we can conclude that the major absorption edge (at 2.08(1) eV) corresponds to the target compound  $\text{Ag}_2\text{SrSiS}_4$  while the foot likely results from small inclusions of poorly crystalline  $\text{Ag}_8\text{SiS}_6$  or a related phase.

**Table 2.** Band gaps and absorption edges from experimental measurement and calculation (DFT-HSE06+SOC,  $\alpha = 0.25$ ). The underestimation of the fundamental band gap by a few tenths of an eV, when computed using this particular density functional parameterization, is consistent with the trend found in our previous studies of  $\text{I}_2\text{-II-IV-X}_4$  materials.<sup>34,38,58,59,74</sup>

Compound	Band gap (eV)		
	HSE06+SOC Indirect	HSE06+SOC Direct	Indirect $\tau_{\text{auc}}$
$\text{Ag}_2\text{SrSiS}_4$	1.75	2.31	2.08(1)
$\text{Ag}_2\text{SrGeS}_4$	1.38	1.84	1.73(2)

The somewhat weak start of absorption seen in the reflectance spectra of each of these isostructural materials could be due to the low density of bands at both the valence and conduction band extrema (**Figure 3**), as well as due to the indirect nature of the associated transitions. While weak light absorption is not favorable for absorber materials in single-junction PV devices, these two compounds are possible candidates for other optoelectronic and optical applications. First, the weak absorption combined with the high degree of band curvature (i.e., prospects of low effective masses and high mobilities) point to possible suitability as lattice- and chemistry-matched PV buffer layers for more appropriate absorber materials within the  $\text{I}_2\text{-II-IV-X}_4$  family, such as  $\text{Ag}_2\text{PbGeS}_4$ .<sup>98</sup> Further, promising NLO candidates within the  $\text{I}_2\text{-II-IV-X}_4$  family have been explored and it has been previously suggested that the combination of larger,

electropositive cation (Sr or Ba) combined with the NLO active [IV-X<sub>4</sub>] units provides a pathway to superior NLO performance.<sup>87</sup> Here, Ag<sub>2</sub>SrSiS<sub>4</sub> and Ag<sub>2</sub>SrGeS<sub>4</sub> both share these properties and therefore may be candidates for NLO applications.

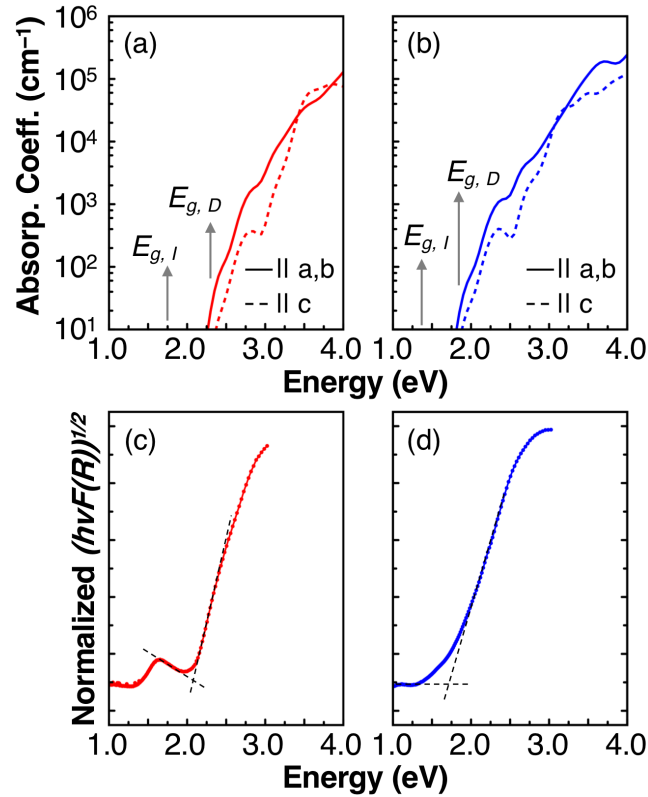


**Figure 4.** Optical properties of the title compounds Ag<sub>2</sub>SrSiS<sub>4</sub> (red) and Ag<sub>2</sub>SrGeS<sub>4</sub> (blue). (a, b) DFT-calculated absorption coefficients using a 0.1 eV Gaussian broadening function. The calculated lowest energy indirect ( $E_{g, I}$ ) and direct ( $E_{g, D}$ ) band gaps are labelled in the figure. Note that phonon-assisted transitions—i.e., indirect transitions—are not included in the calculated absorption coefficients in (a, b). Indirect Tauc plots of the Ag<sub>2</sub>SrSiS<sub>4</sub> (b) and Ag<sub>2</sub>SrGeS<sub>4</sub> (c) reflectance spectra. Fitting lines of the indirect Tauc plots to extract the band gap of Ag<sub>2</sub>SrSiS<sub>4</sub> and Ag<sub>2</sub>SrGeS<sub>4</sub> are shown as dotted black lines.

Alongside the promising structural aspects of the noncentrosymmetric Ag<sub>2</sub>SrSiS<sub>4</sub> and Ag<sub>2</sub>SrGeS<sub>4</sub> for NLO applications, their band gaps also fall between those of the commercial frequency-doubling crystals AgGaSe<sub>2</sub> (1.72 eV) and AgGaS<sub>2</sub> (2.62 eV).<sup>99</sup> To demonstrate the principle of Ag<sub>2</sub>SrSiS<sub>4</sub> and Ag<sub>2</sub>SrGeS<sub>4</sub> as frequency-doubling materials, we measured the SHG intensity of the synthesized powders and compared their performance to that of AgGaS<sub>2</sub>. Each of the samples were excited at 1.8  $\mu\text{m}$  and a SHG signal was measured at 0.9  $\mu\text{m}$ , as shown in **Figure 5**. At this excitation wavelength, the SHG intensities of the Ag<sub>2</sub>SrSiS<sub>4</sub> and Ag<sub>2</sub>SrGeS<sub>4</sub> powders were 0.59 and 0.62 times that of AgGaS<sub>2</sub>. These ratios are roughly equal to the typical performance of other studied members of the I<sub>2</sub>-II-IV-X<sub>4</sub> family with large II atoms that take the  $\bar{I}42m$  structure.<sup>55,60</sup> However, their performances do fall short of other quaternary chalcogenides,<sup>100–</sup>

<sup>102</sup> including the chalcopyrite-derived Li-containing compounds that share the I<sub>2</sub>-II-IV-X<sub>4</sub> stoichiometry as those semiconductors presented here.<sup>103,104</sup> The frequency-doubling measurements demonstrate that Ag<sub>2</sub>SrSiS<sub>4</sub> and Ag<sub>2</sub>SrGeS<sub>4</sub> exhibit near-IR NLO properties. However, further work to grow high-quality cm-scale single crystals is necessary to examine the potential of these materials for optical devices and fully characterize their NLO properties.

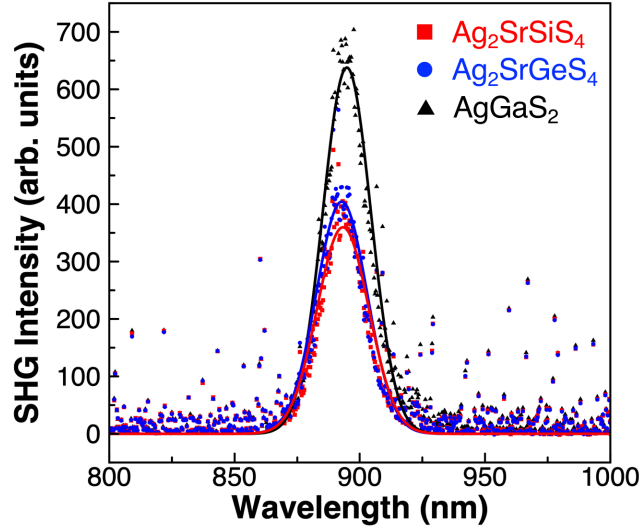


**Figure 5.** Second-harmonic generation of Ag<sub>2</sub>SrSiS<sub>4</sub> (red squares) and Ag<sub>2</sub>SrGeS<sub>4</sub> (blue circles) compared to AgGaS<sub>2</sub> (black triangles). Excitation radiation was centered at 1.8 μm. Gaussian fitting curves of the three spectra are included in the same color as the data.

## Conclusions

Here, we report on the synthesis of bulk powder and single crystal samples of two new quaternary chalcogenide semiconductors Ag<sub>2</sub>SrSiS<sub>4</sub> and Ag<sub>2</sub>SrGeS<sub>4</sub> that fall within the important I<sub>2</sub>-II-IV-X<sub>4</sub> materials family. Ag<sub>2</sub>SrSiS<sub>4</sub> and Ag<sub>2</sub>SrGeS<sub>4</sub> are the first two experimentally studied I<sub>2</sub>-II-IV-X<sub>4</sub> compounds containing both Ag and Sr, furthering the understanding of the phase stability of this materials family and the applicability of the previously developed structural tolerance factor approach.<sup>59</sup> These two compounds are isostructural and demonstrate similar synthetic properties, namely the existence of a competing quaternary phase that can be removed under a SrS-reduced synthesis condition. For a stoichiometric solid-state reaction, two secondary phases form—i.e., Ag<sub>2</sub>Sr<sub>2</sub>Si<sub>3</sub>S<sub>8</sub> and Ag<sub>2</sub>Sr<sub>2</sub>Ge<sub>3</sub>S<sub>8</sub>—in addition to the title compounds. These two secondary phases are isostructural and form in a cubic structure with partially occupied Ag sites. We characterized the electronic structure and optical properties of the title compounds, showing that each of the new semiconductors have highly dispersive band edges with indirect experimental band gaps of 2.08(1) and 1.73(2) eV for Ag<sub>2</sub>SrSiS<sub>4</sub> and Ag<sub>2</sub>SrGeS<sub>4</sub>, respectively. Further, Ag<sub>2</sub>SrSiS<sub>4</sub> and Ag<sub>2</sub>SrGeS<sub>4</sub> are shown to exhibit frequency doubling in the near IR region. The combination of these optoelectronic properties shows that Ag<sub>2</sub>SrSiS<sub>4</sub> and Ag<sub>2</sub>SrGeS<sub>4</sub> are prospective NLO materials.

## Conflicts of Interest

Volker Blum is a member of the executive board of MSIP e.V., the non-profit which licenses the FHI-aims electronic structure code used in this work. Volker Blum does not receive any financial gains from this position. All the other authors have no conflicts to declare.

## Acknowledgements

This material is based upon work supported by the U.S. Department of Energy (DOE), Office of Science, Basic Energy Sciences (BES), under Contract DE-SC0020061. G.C.M.W. acknowledges the support of the National Science Foundation Graduate Research Fellowship Program under Grant DGE-1644868. This research also used resources of the National Energy Research Scientific Computing Center (NERSC), a U.S. (DOE) Office of Science User Facility operated under Contract DE-AC02-05CH11231. Additionally, this work used the Extreme Science and Engineering Discovery Environment (XSEDE), which is supported by National Science Foundation grant number ACI-1548562. The work uses the XSEDE Expanse at the San Diego Supercomputer Center through allocation TG-DMR200077. G.C.M.W. would like to thank Dr. Nelson Rivera for his assistance measuring the elemental composition of samples by ICP-MS and Dr. Manoj Jana for his aid in refining the single crystal structure solutions.

## Supporting Information

Photo of a  $\text{Ag}_2\text{SrGeS}_4$  powder sample; Powder X-ray diffraction and reflectance data for  $\text{Ag}_2\text{SrSiS}_4$  and  $\text{Ag}_2\text{SrGeS}_4$  over time; Crystallographic data for  $\text{Ag}_2\text{SrGeS}_4$ ,  $\text{Ag}_2\text{SrSiS}_4$ , and  $\text{Ag}_2\text{Sr}_3\text{Si}_2\text{S}_8$ ; Lattice parameters and Brillouin zone path used in hybrid density functional theory calculations; Comparison of calculation geometries and experimental data; Structural tolerance factor plot; Powder X-ray diffraction patterns showing impurity phases; Powder X-ray diffraction data for  $\text{Ag}_2\text{SrGeS}_4$  compared to a calculated  $I222$  structure; Powder X-ray diffraction-refined lattice parameters for synthesized materials; Comparison of  $\bar{I}42m$  and  $I222$  crystal structures;  $\text{Ag}_2\text{SrSiS}_4$  crystal structure graphic; Densities of states of  $\text{Ag}_2\text{SrSiS}_4$  and  $\text{Ag}_2\text{SrGeS}_4$  over a wide energy range; Calculated effective mass values of  $\text{Ag}_2\text{SrSiS}_4$  and  $\text{Ag}_2\text{SrGeS}_4$ ; Parameter-optimized calculated band structures; Image of  $\text{Ag}_2\text{SrSiS}_4$  sample and comparison to  $\text{Ag}_8\text{SiS}_6$  reflectance; Geometries of  $\text{Ag}_2\text{SrSiS}_4$  and  $\text{Ag}_2\text{SrGeS}_4$  used in hybrid calculations.

## Data Availability & Accession Codes

The input and output files for the hybrid DFT calculations of electronic band structure (at various  $\alpha$  values), densities of states, and effective masses have been deposited in the online NOMAD repository at <https://dx.doi.org/10.17172/NOMAD/2021.06.27-1>. CCDC 2070439–2070441 contain the supplementary

crystallographic data for this paper. These data can be obtained free of charge via [www.ccdc.cam.ac.uk/data\\_request/cif](http://www.ccdc.cam.ac.uk/data_request/cif), or by emailing [data\\_request@ccdc.cam.ac.uk](mailto:data_request@ccdc.cam.ac.uk), or by contacting The Cambridge Crystallographic Data Centre, 12 Union Road, Cambridge CB2 1EZ, UK; fax: +44 1223 336033.

## References

- (1) Zakutayev, A. Brief Review of Emerging Photovoltaic Absorbers. *Curr. Opin. Green Sustain. Chem.* **2017**, *4*, 8–15.
- (2) Le Donne, A.; Trifiletti, V.; Binetti, S. New Earth-Abundant Thin Film Solar Cells Based on Chalcogenides. *Front. Chem.* **2019**, *7*, 297.
- (3) Woods-Robinson, R.; Han, Y.; Zhang, H.; Ablekim, T.; Khan, I.; Persson, K. A.; Zakutayev, A. Wide Band Gap Chalcogenide Semiconductors. *Chem. Rev.* **2020**, *120*, 4007–4055.
- (4) Chen, M. M.; Xue, H. G.; Guo, S. P. Multinary Metal Chalcogenides with Tetrahedral Structures for Second-Order Nonlinear Optical, Photocatalytic, and Photovoltaic Applications. *Coord. Chem. Rev.* **2018**, *368*, 115–133.
- (5) Yu, Y.; Cagnoni, M.; Cojocaru-Mirédin, O.; Wuttig, M. Chalcogenide Thermoelectrics Empowered by an Unconventional Bonding Mechanism. *Adv. Funct. Mater.* **2020**, *30*, 1904862.
- (6) Wei, T. R.; Qin, Y.; Deng, T.; Song, Q.; Jiang, B.; Liu, R.; Qiu, P.; Shi, X.; Chen, L. Copper Chalcogenide Thermoelectric Materials. *Sci. China Mater.* **2019**, *62*, 8–24.
- (7) Shi, Y.; Sturm, C.; Kleinke, H. Chalcogenides as Thermoelectric Materials. *J. Solid State Chem.* **2019**, *270*, 273–279.
- (8) Lin, H.; Wei, W. B.; Chen, H.; Wu, X. T.; Zhu, Q. L. Rational Design of Infrared Nonlinear Optical Chalcogenides by Chemical Substitution. *Coord. Chem. Rev.* **2020**, *406*, 213150.
- (9) Wu, K.; Pan, S. A Review on Structure-Performance Relationship toward the Optimal Design of Infrared Nonlinear Optical Materials with Balanced Performances. *Coord. Chem. Rev.* **2018**, *377*, 191–208.
- (10) Guo, S.-P.; Chi, Y.; Guo, G.-C. Recent Achievements on Middle and Far-Infrared Second-Order Nonlinear Optical Materials. *Coord. Chem. Rev.* **2017**, *335*, 44–57.
- (11) Eggleton, B. J.; Luther-Davies, B.; Richardson, K. Chalcogenide Photonics. *Nat. Photonics* **2011**, *5*, 141–148.
- (12) Green, M. A.; Dunlop, E. D.; Hohl-Ebinger, J.; Yoshita, M.; Kopidakis, N.; Ho-Baillie, A. W. Y. Solar Cell Efficiency Tables (Version 55). *Prog Photovolt Res Appl.* **2020**, *28*, 3–15.
- (13) Systems, F. I. for S. E. Photovoltaics Report <https://www.ise.fraunhofer.de/content/dam/ise/de/documents/publications/studies/Photovoltaics-Report.pdf> (accessed Jan 22, 2021).
- (14) Okorogu, A. O.; Mirov, S. B.; Lee, W.; Crouthamel, D. I.; Jenkins, N.; Dergachev, A. Y.; Vodopyanov, K. L.; Badikov, V. V. Tunable Middle Infrared Downconversion in GaSe and AgGaS<sub>2</sub>. *Opt. Commun.* **1998**, *155*, 307–312.
- (15) Boyd, G. D.; Kasper, H. M.; McFee, J. H.; Storz, F. G. Linear and Nonlinear Optical Properties of Some Ternary Selenides. *IEEE J. Quantum Electron.* **1972**, *8*, 900–908.
- (16) Chu, Y.; Li, G.; Su, X.; Wu, K.; Pan, S. A Review on the Development of Infrared Nonlinear Optical Materials with Triangular Anionic Groups. *J. Solid State Chem.* **2019**, *271*, 266–272.
- (17) Liang, F.; Kang, L.; Lin, Z.; Wu, Y.; Chen, C. Analysis and Prediction of Mid-IR Nonlinear Optical Metal Sulfides with Diamond-like Structures. *Coord. Chem. Rev.* **2017**, *333*, 57–70.
- (18) Gokmen, T.; Gunawan, O.; Todorov, T. K.; Mitzi, D. B. Band Tailing and Efficiency Limitation in Kesterite Solar Cells. *Appl. Phys. Lett.* **2013**, *103*, 103506.
- (19) Chen, S.; Walsh, A.; Gong, X. G.; Wei, S. H. Classification of Lattice Defects in the Kesterite Cu<sub>2</sub>ZnSnS<sub>4</sub> and Cu<sub>2</sub>ZnSnSe<sub>4</sub> Earth-Abundant Solar Cell Absorbers. *Adv. Mater.* **2013**, *25*, 1522–1539.
- (20) Chen, S.; Gong, X. G.; Walsh, A.; Wei, S. H. Defect Physics of the Kesterite Thin-Film Solar Cell Absorber Cu<sub>2</sub>ZnSnS<sub>4</sub>. *Appl. Phys. Lett.* **2010**, *96*, 021902.
- (21) Rudisch, K.; Davydova, A.; Platzer-Björkman, C.; Scragg, J. The Effect of Stoichiometry on Cu-Zn Ordering Kinetics in Cu<sub>2</sub>ZnSnS<sub>4</sub> Thin Films. *J. Appl. Phys.* **2018**, *123*, 161558.
- (22) Wang, W.; Winkler, M. T.; Gunawan, O.; Gokmen, T.; Todorov, T. K.; Zhu, Y.; Mitzi, D. B. Device

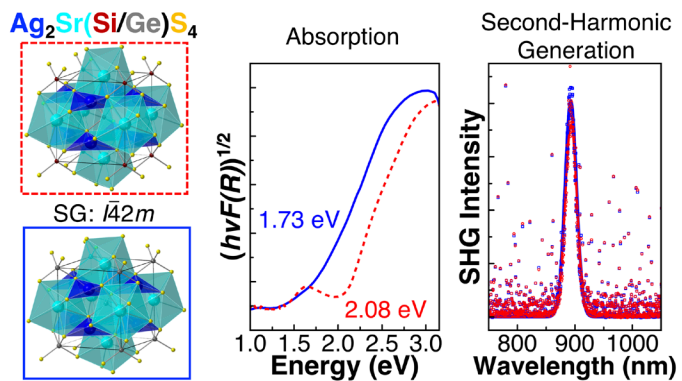
- Characteristics of CZTSSe Thin-Film Solar Cells with 12.6% Efficiency. *Adv. Energy Mater.* **2014**, *4*, 1301465.
- (23) Olekseyuk, I. D.; Dudchak, I. V.; Piskach, L. V. Phase Equilibria in the  $\text{Cu}_2\text{S}-\text{ZnS}-\text{SnS}_2$  System. *J. Alloys Compd.* **2004**, *368*, 135–143.
- (24) Dudchak, I. V.; Piskach, L. V. Phase Equilibria in the  $\text{Cu}_2\text{SnSe}_3-\text{SnSe}_2-\text{ZnSe}$  System. *J. Alloys Compd.* **2003**, *351*, 145–150.
- (25) Scragg, J. J.; Ericson, T.; Kubart, T.; Edoff, M.; Platzer-Björkman, C. Chemical Insights into the Instability of  $\text{Cu}_2\text{ZnSnS}_4$  Films during Annealing. *Chem. Mater.* **2011**, *23*, 4625–4633.
- (26) Rey, G.; Redinger, A.; Sendler, J.; Weiss, T. P.; Thevenin, M.; Guennou, M.; El Adib, B.; Siebentritt, S. The Band Gap of  $\text{Cu}_2\text{ZnSnSe}_4$ : Effect of Order-Disorder. *Appl. Phys. Lett.* **2014**, *105*, 112106.
- (27) Krämer, C.; Huber, C.; Zimmermann, C.; Lang, M.; Schnabel, T.; Abzieher, T.; Ahlswede, E.; Kalt, H.; Hetterich, M. Reversible Order-Disorder Related Band Gap Changes in  $\text{Cu}_2\text{ZnSn}(\text{S},\text{Se})_4$  via Post-Annealing of Solar Cells Measured by Electroreflectance. *Appl. Phys. Lett.* **2014**, *105*, 262104.
- (28) Scragg, J. J.; Larsen, J. K.; Kumar, M.; Persson, C.; Sendler, J.; Siebentritt, S.; Platzer Björkman, C. Cu-Zn Disorder and Band Gap Fluctuations in  $\text{Cu}_2\text{ZnSn}(\text{S},\text{Se})_4$ : Theoretical and Experimental Investigations. *Phys. Status Solidi Basic Res.* **2016**, *253*, 247–254.
- (29) Hages, C. J.; Levenco, S.; Miskin, C. K.; Alsmeyer, J. H.; Abou-Ras, D.; Wilks, R. G.; Bär, M.; Unold, T.; Agrawal, R. Improved Performance of Ge-alloyed CZTGeSSe Thin-film Solar Cells through Control of Elemental Losses. *Prog. Photovoltaics Res. Appl.* **2015**, *23*, 376–384.
- (30) Hadke, S. H.; Levchenko, S.; Lie, S.; Hages, C. J.; Márquez, J. A.; Unold, T.; Wong, L. H. Synergistic Effects of Double Cation Substitution in Solution-Processed CZTS Solar Cells with over 10 % Efficiency. *Adv. Energy Mater.* **2018**, *1802540*, 1802540.
- (31) Kim, S.; Kim, K. M.; Tampo, H.; Shibata, H.; Niki, S. Improvement of Voltage Deficit of Ge-Incorporated Kesterite Solar Cell with 12.3% Conversion Efficiency. *Appl. Phys. Express* **2016**, *9*, 102301.
- (32) Giraldo, S.; Thersleff, T.; Larramona, G.; Neuschitzer, M.; Pistor, P.; Leifer, K.; Perez-Rodriguez, A.; Moisan, C.; Dennler, G.; Saucedo, E.  $\text{Cu}_2\text{ZnSnSe}_4$  Solar Cells with 10.6% Efficiency through Innovative Absorber Engineering with Ge Superficial Nanolayer. *Prog Photovolt Res Appl.* **2016**, *24*, 1359–1367.
- (33) Yuan, Z. K.; Chen, S.; Xiang, H.; Gong, X. G.; Walsh, A.; Park, J. S.; Repins, I. L.; Wei, S. H. Engineering Solar Cell Absorbers by Exploring the Band Alignment and Defect Disparity: The Case of Cu- and Ag-Based Kesterite Compounds. *Adv. Funct. Mater.* **2015**, *25*, 6733–6743.
- (34) Shin, D.; Saporov, B.; Zhu, T.; Huhn, W. P.; Blum, V.; Mitzi, D. B.  $\text{BaCu}_2\text{Sn}(\text{S},\text{Se})_4$  – Earth-Abundant Chalcogenides for Thin-Film Photovoltaics. *Chem. Mater.* **2016**, *28*, 4771–4780.
- (35) Hong, F.; Lin, W.; Meng, W.; Yan, Y. Trigonal  $\text{Cu}_2\text{-II-Sn-VI}_4$  (II = Ba, Sr and VI = S, Se) Quaternary Compounds for Earth-Abundant Photovoltaics. *Phys. Chem. Chem. Phys.* **2016**, *18*, 4828–4834.
- (36) Shin, D.; Saporov, B.; Mitzi, D. B. Defect Engineering in Multinary Earth-Abundant Chalcogenide Photovoltaic Materials. *Adv. Energy Mater.* **2017**, *7*, 1602366.
- (37) Teske, C. L.; Vetter, O. Präparative Und Röntgenographische Untersuchung Am System  $\text{Cu}_{2-x}\text{Ag}_x\text{BaSnS}_4$ . *Z. Anorg. Allg. Chem.* **1976**, *426*, 281–287.
- (38) Shin, D.; Zhu, T.; Huang, X.; Gunawan, O.; Blum, V.; Mitzi, D. B. Earth-Abundant Chalcogenide Photovoltaic Devices with over 5% Efficiency Based on a  $\text{Cu}_2\text{BaSn}(\text{S},\text{Se})_4$  Absorber. *Adv. Mater.* **2017**, *29*, 1606945.
- (39) Ge, J.; Koirala, P.; Grice, C. R.; Roland, P. J.; Yu, Y.; Tan, X.; Ellingson, R. J.; Collins, R. W.; Yan, Y. Oxygenated CdS Buffer Layers Enabling High Open-Circuit Voltages in Earth-Abundant  $\text{Cu}_2\text{BaSnS}_4$  Thin-Film Solar Cells. *Adv. Energy Mater.* **2017**, *7*, 1601803.
- (40) Crovetto, A.; Børsting, K.; Nielsen, R.; Hajjifarassat, A.; Hansen, O.; Seger, B.; Chorkendorff, I.; Vesborg, P. C. K.  $\text{TaS}_2$  Back Contact Improving Oxide-Converted  $\text{Cu}_2\text{BaSnS}_4$  Solar Cells. *ACS Appl. Energy Mater.* **2020**, *3*, 1190–1198.
- (41) Cui, Y.; Tong, J.; Shao, H.; Wang, G.; Pan, D. Novel  $\text{Cu}_2\text{BaSn}(\text{S},\text{Se})_4$  Thin Film Fabricated by Solution Process and Its Application in Solar Cells. *Superlattices Microstruct.* **2019**, *135*, 106243.
- (42) Chen, Z.; Sun, K.; Su, Z.; Liu, F.; Tang, D.; Xiao, H.; Shi, L.; Jiang, L.; Hao, X.; Lai, Y. Solution-Processed Trigonal  $\text{Cu}_2\text{BaSnS}_4$  Thin-Film Solar Cells. *ACS Appl. Energy Mater.* **2018**, *1*, 3420–3427.
- (43) Luo, H.; Chen, J.; Zhang, X.; Wang, S.; Gu, H.; Wang, W.; Li, H. Controlled Synthesis of High Efficiency  $\text{Cu}_2\text{BaSnS}_4$  Solar Cells via a Solution Processed Method. *Mater. Lett.* **2020**, *270*, 127750.
- (44) Zhou, Y.; Shin, D.; Ngaboyamahina, E.; Han, Q.; Parker, C. B.; Mitzi, D. B.; Glass, J. T. Efficient and Stable  $\text{Pt/TiO}_2/\text{CdS}/\text{Cu}_2\text{BaSn}(\text{S},\text{Se})_4$  Photocathode for Water Electrolysis Applications. *ACS Energy Lett.* **2018**, *3*, 177–183.

- (45) Shin, D.; Ngaboyamahina, E.; Zhou, Y.; Glass, J. T.; Mitzi, D. B. Synthesis and Characterization of an Earth-Abundant  $\text{Cu}_2\text{BaSn}(\text{S},\text{Se})_4$  Chalcogenide for Photoelectrochemical Cell Application. *J. Phys. Chem. Lett.* **2016**, *7*, 4554–4561.
- (46) Teymur, B.; Zhou, Y.; Ngaboyamahina, E.; Glass, J. T.; Mitzi, D. B. Solution-Processed Earth-Abundant  $\text{Cu}_2\text{BaSn}(\text{S},\text{Se})_4$  Solar Absorber Using a Low-Toxicity Solvent. *Chem. Mater.* **2018**, *30*, 6116–6123.
- (47) Ge, J.; Yu, Y.; Yan, Y. Earth-Abundant Trigonal  $\text{BaCu}_2\text{Sn}(\text{Se}_x\text{S}_{1-x})_4$  ( $x = 0-0.55$ ) Thin Films with Tunable Band Gaps for Solar Water Splitting. *J. Mater. Chem. A* **2016**, *4*, 18885–18891.
- (48) Ge, J.; Yu, Y.; Yan, Y. Earth-Abundant Orthorhombic  $\text{BaCu}_2\text{Sn}(\text{Se}_x\text{S}_{1-x})_4$  ( $x \approx 0.83$ ) Thin Film for Solar Energy Conversion. *ACS Energy Lett.* **2016**, *1*, 583–588.
- (49) Ge, J.; Roland, P. J.; Koirala, P.; Meng, W.; Young, J. L.; Petersen, R.; Deutsch, T. G.; Teeter, G.; Ellingson, R. J.; Collins, R. W.; et al. Employing Overlayers To Improve the Performance of  $\text{Cu}_2\text{BaSnS}_4$  Thin Film Based Photoelectrochemical Water Reduction Devices. *Chem. Mater.* **2017**, *29*, 916–920.
- (50) Xie, J.; Yi, Q.; Zhang, F.; Bagheri, R.; Zheng, F.; Zou, G. Large-Grained  $\text{Cu}_2\text{BaSnS}_4$  Films for Photocathodes. *ACS Appl. Mater. Interfaces* **2019**, *11*, 33102–33108.
- (51) M, S. K.; Madhusudanan, S. P.; Kanth, S. C.; Mohanta, K.; Batabyal, S. K. Solution Phase Fabrication of Photoactive  $\text{Cu}_2\text{BaSnS}_4$  Thin Films for Solar Energy Harvesting. *J. Solid State Electrochem.* **2020**, *24*, 305–311.
- (52) Hong, A. J.; Yuan, C. L.; Liu, J. M. Quaternary Compounds  $\text{Ag}_2\text{XYSe}_4$  ( $X=\text{Ba}, \text{Sr}$ ;  $Y=\text{Sn}, \text{Ge}$ ) as Novel Potential Thermoelectric Materials. *J. Phys. D. Appl. Phys.* **2020**, *53*, 115302.
- (53) Kuo, J. J.; Aydemir, U.; Pöhls, J. H.; Zhou, F.; Yu, G.; Faghaninia, A.; Ricci, F.; White, M. A.; Rignanese, G. M.; Hautier, G.; et al. Origins of Ultralow Thermal Conductivity in 1-2-1-4 Quaternary Selenides. *J. Mater. Chem. A* **2019**, *7*, 2589–2596.
- (54) Li, Y.; Li, Z.; Zhang, C.; Yang, D.; Liu, T.; Yan, Y.; Liu, W.; Tan, G.; Su, X.; Uher, C.; et al. Ultralow Thermal Conductivity of  $\text{BaAg}_2\text{SnSe}_4$  and the Effect of Doping by Ga and In. *Mater. Today Phys.* **2019**, *9*, 100098.
- (55) Yang, Y.; Wu, K.; Wu, X.; Zhang, B.; Gao, L. A New Family of Quaternary Thiosilicates  $\text{SrA}_2\text{SiS}_4$  ( $A = \text{Li}, \text{Na}, \text{Cu}$ ) as Promising Infrared Nonlinear Optical Crystals. *J. Mater. Chem. C* **2020**, *8*, 1762–1767.
- (56) Yang, Y.; Wu, K.; Zhang, B.; Wu, X.; Lee, M.-H. Infrared Nonlinear Optical Polymorphs  $\alpha$ - and  $\beta$ - $\text{SrCu}_2\text{SnS}_4$  Exhibiting Large Second Harmonic Generation Responses with Requisite Phase-Matching Behavior. *Chem. Mater.* **2020**, *32*, 1281–1287.
- (57) Chen, H.; Liu, P. F.; Li, B. X.; Lin, H.; Wu, L. M.; Wu, X. T. Experimental and Theoretical Studies on the NLO Properties of Two Quaternary Non-Centrosymmetric Chalcogenides:  $\text{BaAg}_2\text{GeS}_4$  and  $\text{BaAg}_2\text{SnS}_4$ . *Dalt. Trans.* **2018**, *47*, 429–437.
- (58) Zhu, T.; Huhn, W. P.; Wessler, G. C.; Shin, D.; Saparov, B.; Mitzi, D. B.; Blum, V.  $\text{I}_2\text{-II-IV-VI}_4$  ( $\text{I} = \text{Cu}, \text{Ag}$ ;  $\text{II} = \text{Sr}, \text{Ba}$ ;  $\text{IV} = \text{Ge}, \text{Sn}$ ;  $\text{VI} = \text{S}, \text{Se}$ ): Chalcogenides for Thin-Film Photovoltaics. *Chem. Mater.* **2017**, *29*, 7868–7879.
- (59) Sun, J.-P. J.-P.; McKeown Wessler, G. C.; Wang, T.; Zhu, T.; Blum, V.; Mitzi, D. B. Structural Tolerance Factor Approach to Defect-Resistant  $\text{I}_2\text{-II-IV-X}_4$  Semiconductor Design. *Chem. Mater.* **2020**, *32*, 1636–1649.
- (60) Nian, L.; Wu, K.; He, G.; Yang, Z.; Pan, S. Effect of Element Substitution on Structural Transformation and Optical Performances in  $\text{I}_2\text{BaM}^{\text{IV}}\text{Q}_4$  ( $\text{I} = \text{Li}, \text{Na}, \text{Cu}$ , and  $\text{Ag}$ ;  $\text{M}^{\text{IV}} = \text{Si}, \text{Ge}$ , and  $\text{Sn}$ ;  $\text{Q} = \text{S}$  and  $\text{Se}$ ). *Inorg. Chem.* **2018**, *57*, 3434–3442.
- (61) Teske, C. L. Darstellung Und Kristallstruktur von Silber-Barium-Thiogermanat(IV).  $\text{Ag}_2\text{BaGeS}_4$ . *Zeitschrift für Naturforsch., Tl. B Anorg. Chemie, Org. Chemie* **1979**, *34*, 544–547.
- (62) Yang, Y.; Song, M.; Zhang, J.; Gao, L.; Wu, X.; Wu, K. Coordinated Regulation on Critical Physiochemical Performances Activated from Mixed Tetrahedral Anionic Ligands in New Series of  $\text{Sr}_6\text{A}_4\text{M}_4\text{S}_{16}$  ( $A = \text{Ag}, \text{Cu}$ ;  $M = \text{Ge}, \text{Sn}$ ) Nonlinear Optical Materials. *Dalt. Trans.* **2020**, *49*, 3388–3392.
- (63) Sato, T.; Toda, S.; Tachikawa, T. Phase Diagrams of the  $\text{NaI-KI}$  and  $\text{KI-CsI}$  Binary Systems. *Denki Kagaku oyobi Kogyo Butsuri Kagaku* **1987**, *55*, 617–620.
- (64) Makuła, P.; Pacia, M.; Macyk, W. How To Correctly Determine the Band Gap Energy of Modified Semiconductor Photocatalysts Based on UV-Vis Spectra. *J. Phys. Chem. Lett.* **2018**, *9*, 6814–6817.
- (65) Morozov, O. A.; Naumov, A. K.; Lovchev, A. V.; Garipov, M. R. Analysis of Nonlinear Optical Materials Properties by Simple Powder Technique. *J. Phys. Conf. Ser.* **2015**, *594*, 012037.
- (66) Jensen, S. R.; Saha, S.; Flores-Livas, J. A.; Huhn, W.; Blum, V.; Goedecker, S.; Frediani, L. The Elephant in the Room of Density Functional Theory Calculations. *J. Phys. Chem. Lett.* **2017**, *8*, 1449–1457.
- (67) Lejaeghere, K.; Bihlmayer, G.; Bjorkman, T.; Blaha, P.; Blugel, S.; Blum, V.; Caliste, D.; Castelli, I. E.;

- Clark, S. J.; Dal Corso, A.; et al. Reproducibility in Density Functional Theory Calculations of Solids. *Science*. **2016**, *351*, 1415.
- (68) Blum, V.; Gehrke, R.; Hanke, F.; Havu, P.; Havu, V.; Ren, X.; Reuter, K.; Scheffler, M. Ab Initio Molecular Simulations with Numeric Atom-Centered Orbitals. *Comput. Phys. Commun.* **2009**, *180*, 2175–2196.
- (69) Ren, X.; Rinke, P.; Blum, V.; Wieferink, J.; Tkatchenko, A.; Sanfilippo, A.; Reuter, K.; Scheffler, M. Resolution-of-Identity Approach to Hartree-Fock, Hybrid Density Functionals, RPA, MP2 and GW with Numeric Atom-Centered Orbital Basis Functions. *New J. Phys.* **2012**, *14*, 053020.
- (70) Havu, V.; Blum, V.; Havu, P.; Scheffler, M. Efficient O(N) Integration for All-Electron Electronic Structure Calculation Using Numeric Basis Functions. *J. Comput. Phys.* **2009**, *228*, 8367–8379.
- (71) Knuth, F.; Carbogno, C.; Atalla, V.; Blum, V.; Scheffler, M. All-Electron Formalism for Total Energy Strain Derivatives and Stress Tensor Components for Numeric Atom-Centered Orbitals. *Comput. Phys. Commun.* **2015**, *190*, 33–50.
- (72) Levchenko, S. V.; Ren, X.; Wieferink, J.; Johanni, R.; Rinke, P.; Blum, V.; Scheffler, M. Hybrid Functionals for Large Periodic Systems in an All-Electron, Numeric Atom-Centered Basis Framework. *Comput. Phys. Commun.* **2015**, *192*, 60–69.
- (73) Ihrig, A. C.; Wieferink, J.; Zhang, I. Y.; Ropo, M.; Ren, X.; Rinke, P.; Scheffler, M.; Blum, V. Accurate Localized Resolution of Identity Approach for Linear-Scaling Hybrid Density Functionals and for Many-Body Perturbation Theory. *New J. Phys.* **2015**, *17*, 093020.
- (74) Wessler, G. C.; Zhu, T.; Sun, J.-P.; Harrell, A.; Huhn, W. P.; Blum, V.; Mitzi, D. B. Band Gap Tailoring and Structure-Composition Relationship within the Alloyed Semiconductor  $\text{Cu}_2\text{BaGe}_{1-x}\text{Sn}_x\text{Se}_4$ . *Chem. Mater.* **2018**, *30*, 6566–6574.
- (75) Heyd, J.; Scuseria, G. E.; Ernzerhof, M. Hybrid Functionals Based on a Screened Coulomb Potential. *J. Chem. Phys.* **2003**, *118*, 8207–8215.
- (76) Krukau, A. V.; Vydrov, O. A.; Izmaylov, A. F.; Scuseria, G. E. Influence of the Exchange Screening Parameter on the Performance of Screened Hybrid Functionals. *J. Chem. Phys.* **2006**, *125*, 224106.
- (77) Heyd, J.; Scuseria, G. E.; Ernzerhof, M. Erratum: Hybrid Functionals Based on a Screened Coulomb Potential (Journal of Chemical Physics (2003) 118 (8207)). *J. Chem. Phys.* **2006**, *124*, 219906.
- (78) Perdew, J. P.; Yang, W.; Burke, K.; Yang, Z.; Gross, E. K. U.; Scheffler, M.; Scuseria, G. E.; Henderson, T. M.; Zhang, I. Y.; Ruzsinszky, A.; et al. Understanding Band Gaps of Solids in Generalized Kohn–Sham Theory. *Proc. Natl. Acad. Sci.* **2017**, *114*, 2801–2806.
- (79) Botti, S.; Kammerlander, D.; Marques, M. A. L. Band Structures of  $\text{Cu}_2\text{ZnSnS}_4$  and  $\text{Cu}_2\text{ZnSnSe}_4$  from Many-Body Methods. *Appl. Phys. Lett.* **2011**, *98*, 241915.
- (80) Huhn, W. P.; Blum, V. One-Hundred-Three Compound Band-Structure Benchmark of Post-Self-Consistent Spin-Orbit Coupling Treatments in Density Functional Theory. *Phys. Rev. Mater.* **2017**, *1*, 033803.
- (81) MacDonald, A. H.; Vosko, S. H.; Coleridge, P. T. Extensions of the Tetrahedron Method for Evaluating Spectral Properties of Solids. *J. Phys. C Solid State Phys.* **1979**, *12*, 2991–3002.
- (82) Ashcroft, N. W.; Mermin, N. D. *Solid State Physics*; Saunders College Publishing: Fort Worth, TX, USA, 1976.
- (83) Ambrosch-Draxl, C.; Sofo, J. O. Linear Optical Properties of Solids within the Full-Potential Linearized Augmented Planewave Method. *Comput. Phys. Commun.* **2006**, *175*, 1–14.
- (84) Teske, C. L. Über Die Darstellung Und Röntgenographische Untersuchung von  $\text{Cu}_2\text{SrGeS}_4$  Und  $\text{Cu}_2\text{BaGeS}_4$ . *Zeitschrift für Naturforsch B* **1979**, *34*, 386–389.
- (85) Teske, C. L. Darstellung Und Kristallstruktur von  $\text{Cu}_2\text{SrSnS}_4$ . *Z. Anorg. Allg. Chem.* **1976**, *419*, 67–76.
- (86) Wu, K.; Zhang, B.; Yang, Z.; Pan, S. New Compressed Chalcopyrite-like  $\text{Li}_2\text{BaM}^{\text{IV}}\text{Q}_4$  ( $\text{M}^{\text{IV}} = \text{Ge, Sn}$ ;  $\text{Q} = \text{S, Se}$ ): Promising Infrared Nonlinear Optical Materials. *J. Am. Chem. Soc.* **2017**, *139*, 14885–14888.
- (87) Wu, K.; Chu, Y.; Yang, Z.; Pan, S.  $\text{A}_2\text{SrM}^{\text{IV}}\text{S}_4$  ( $\text{A} = \text{Li, Na}$ ;  $\text{M}^{\text{IV}} = \text{Ge, Sn}$ ) Concurrently Exhibiting Wide Bandgaps and Good Nonlinear Optical Responses as New Potential Infrared Nonlinear Optical Materials. *Chem. Sci.* **2019**, *10*, 3963–3968.
- (88) Tampier, M. Chalkogenogermanate Der Übergangselemente Mit Unedlen Metallen, Heinrich-Heine-Universität Düsseldorf, Germany, 2002.
- (89) Márquez, J. A.; Sun, J.-P.; Stange, H.; Ali, H.; Choubrac, L.; Schäfer, S.; Hages, C. J.; Leifer, K.; Unold, T.; Mitzi, D. B.; et al. High-Temperature Decomposition of  $\text{Cu}_2\text{BaSnS}_4$  with Sn Loss Reveals Newly Identified Compound  $\text{Cu}_2\text{Ba}_3\text{Sn}_2\text{S}_8$ . *J. Mater. Chem. A* **2020**, *8*, 11346–11353.
- (90) Robbins, M.; Miksovsky, M. A. Preparation of and Phase Relationships in Systems of the Type  $\text{ZnS-M}^{\text{I}}\text{M}^{\text{III}}\text{S}_2$  Where  $\text{M}^{\text{I}} = \text{Cu, Ag}$  and  $\text{M}^{\text{III}} = \text{In, Ga, Al}$ . *J. Solid State Chem.* **1972**, *5*, 462–466.
- (91) Gong, W.; Tabata, T.; Takei, K.; Morihama, M.; Maeda, T.; Wada, T. Crystallographic and Optical

- Properties of  $(\text{Cu}, \text{Ag})_2\text{ZnSnS}_4$  and  $(\text{Cu}, \text{Ag})_2\text{ZnSnSe}_4$  Solid Solutions. *Phys. Status Solidi* **2015**, *12*, 700–703.
- (92) Tampier, M.; Johrendt, D. Neue Azentrische Selenogermanate. I. Kristallstrukturen Und Chemische Bindung von  $\text{AM}_2\text{GeSe}_4$  ( $\text{A} = \text{Sr}, \text{Ba}$ ;  $\text{M} = \text{Cu}, \text{Ag}$ ). *Z. Anorg. Allg. Chem.* **2001**, *627*, 312–320.
- (93) Teske, C. L.; Vetter, O. Ergebnisse Einer Rontgenstrukturanalyse von Silber-Barium-Thiostannat(IV),  $\text{Ag}_2\text{BaSnS}_4$ . *Z. Anorg. Allg. Chem.* **1976**, *427*, 200–204.
- (94) Assoud, A.; Soheilnia, N.; Kleinke, H. New Quaternary Barium Copper/Silver Selenostannates: Different Coordination Spheres, Metal-Metal Interactions, and Physical Properties. *Chem. Mater.* **2005**, *17*, 2255–2261.
- (95) Vitale, S. A.; Nezich, D.; Varghese, J. O.; Kim, P.; Gedik, N.; Jarillo-Herrero, P.; Xiao, D.; Rothschild, M. Valleytronics: Opportunities, Challenges, and Paths Forward. *Small* **2018**, *14*, 1801483.
- (96) Norouzzadeh, P.; Shakouri, A.; Vashaee, D. Valleytronics of III-V Solid Solutions for Thermoelectric Application. *RSC Adv.* **2017**, *7*, 7310–7314.
- (97) Peng, H.; Gu, N.; Machida, N.; Shigematsu, T. High  $\text{Ag}_2\text{S}$ -Containing Amorphous Materials in the System  $\text{Ag}_2\text{S}$ - $\text{SiS}_2$  and Their Electrical Properties. *Electrochim. Acta* **2003**, *48*, 1893–1897.
- (98) Nhalil, H.; Han, D.; Du, M.-H.; Chen, S.; Antonio, D.; Gofryk, K.; Saparov, B. Optoelectronic Properties of Candidate Photovoltaic  $\text{Cu}_2\text{PbSiS}_4$ ,  $\text{Ag}_2\text{PbGeS}_4$ , and  $\text{KAgl}_2\text{SbS}_4$  Semiconductors. *J. Alloys Compd.* **2018**, *746*, 405–412.
- (99) Bhar, G. C.; Smith, R. C. Optical Properties of II–IV– $\text{V}_2$  and I–III– $\text{VI}_2$  Crystals with Particular Reference to Transmission Limits. *Phys. Status Solidi* **1972**, *13*, 157–168.
- (100) Li, G.; Wu, K.; Liu, Q.; Yang, Z.; Pan, S.  $\text{Na}_2\text{ZnGe}_2\text{S}_6$ : A New Infrared Nonlinear Optical Material with Good Balance between Large Second-Harmonic Generation Response and High Laser Damage Threshold. *J. Am. Chem. Soc.* **2016**, *138*, 7422–7428.
- (101) Lin, Y. J.; Liu, B. W.; Ye, R.; Jiang, X. M.; Yang, L. Q.; Zeng, H. Y.; Guo, G. C.  $\text{SrCdSnQ}_4$  ( $\text{Q} = \text{S}$  and  $\text{Se}$ ): Infrared Nonlinear Optical Chalcogenides with Mixed NLO-Active and Synergetic Distorted Motifs. *J. Mater. Chem. C* **2019**, *7*, 4459–4465.
- (102) Guo, Y.; Liang, F.; Yin, W.; Li, Z.; Luo, X.; Lin, Z. S.; Yao, J.; Mar, A.; Wu, Y.  $\text{BaHgGeSe}_4$  and  $\text{SrHgGeSe}_4$ : Two New Hg-Based Infrared Nonlinear Optical Materials. *Chem. Mater.* **2019**, *31*, 3034–3040.
- (103) Li, G. M.; Chu, Y.; Li, J.; Zhou, Z. X.  $\text{Li}_2\text{CdSiS}_4$ , a Promising IR NLO Material with a Balanced  $E_g$  and SHG Response Originating from the Effect of Cd with  $d^{10}$  Configuration. *Dalt. Trans.* **2020**, *49*, 1975–1980.
- (104) Zhang, J. H.; Clark, D. J.; Brant, J. A.; Rosmus, K. A.; Grima, P.; Lekse, J. W.; Jang, J. I.; Aitken, J. A.  $\text{A-Li}_2\text{ZnGeS}_4$ : A Wide-Bandgap Diamond-like Semiconductor with Excellent Balance between Laser-Induced Damage Threshold and Second Harmonic Generation Response. *Chem. Mater.* **2020**, *32*, 8947–8955.

## For Table of Contents Only



Two new quaternary sulfide semiconductors— $\text{Ag}_2\text{SrSiS}_4$  and  $\text{Ag}_2\text{SrGeS}_4$ —are synthesized and structurally characterized. The calculated band structures and measured absorption and nonlinear optical spectra show that  $\text{Ag}_2\text{SrSiS}_4$  and  $\text{Ag}_2\text{SrGeS}_4$  are prospective frequency-doubling compounds in the near-infrared region.